

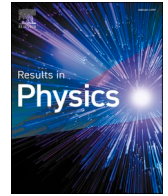
VALIZADEH, S., SHOKRI, A., SABOURI-DODARAN, A., FOUGH, N. and MUHAMMAD-SUKKI, F. 2024. Investigation of efficiency and temperature dependence in RbGeBr<sub>3</sub>-based perovskite solar cell structures. *Results in physics* [online], 57, article 107351. Available from: <https://doi.org/10.1016/j.rinp.2024.107351>

# Investigation of efficiency and temperature dependence in RbGeBr<sub>3</sub>-based perovskite solar cell structures.

VALIZADEH, S., SHOKRI, A., SABOURI-DODARAN, A., FOUGH, N. and MUHAMMAD-SUKKI, F.

2024

© 2024 The Author(s). Published by Elsevier B.V. This is an open access article under the CC BY-NC-ND license (<http://creativecommons.org/licenses/by-nc-nd/4.0/>).



# Investigation of efficiency and temperature dependence in RbGeBr<sub>3</sub>-based perovskite solar cell structures

Shima Valizadeh<sup>a</sup>, Aliasghar Shokri<sup>b,\*</sup>, Amirabbas Sabouri-Dodaran<sup>a</sup>, Nazila Fough<sup>c</sup>, Firdaus Muhammad-Sukki<sup>d</sup>

<sup>a</sup> Department of Physics, Payame Noor University (PNU), Tehran, Iran

<sup>b</sup> Department of Theoretical Physics and Nano, Faculty of Physics, Alzahra University, Tehran, Iran

<sup>c</sup> School of Engineering, Robert Gordon University, The Sir Ian Wood Building, Garthdee Road, Garthdee, Aberdeen AB10 7JG, United Kingdom

<sup>d</sup> School of Computing, Engineering & the Built Environment, Edinburgh Napier University, 10 Colinton Road, Edinburgh EH10 5DT, United Kingdom

## ARTICLE INFO

### Keywords:

Perovskite solar cell  
Photovoltaic  
Inorganic absorber layer  
Efficiency  
COMSOL Multiphysics simulator

## ABSTRACT

This study is centered on the exploration of the inorganic perovskite material RbGeBr<sub>3</sub> as an absorbing layer in various configurations of perovskite solar cells (PSCs). The Poisson, continuity, and transport equations are solved using the finite element method for calculation. Systematic variations in the thicknesses of the RbGeBr<sub>3</sub> absorber layer and the electron transfer layer are performed, with gold (Au) and silver (Ag) utilized as metal contacts for the electrodes. The study also delves into the impact of temperature variations on the efficacy of these structures. Among the tested configurations, the FTO/TiO<sub>2</sub>/RbGeBr<sub>3</sub>/P<sub>3</sub>HT/Au configuration emerges as the most efficient, achieving a power conversion efficiency of 11.89%, with a short-circuit current of 14.47 mA/cm<sup>2</sup> and an open-circuit voltage of 0.96 V. Additionally, two alternative structures, FTO/ITO/RbGeBr<sub>3</sub>/PEDOT:PSS/Au and FTO/ITO/RbGeBr<sub>3</sub>/PEDOT:PSS/Ag, are investigated, yielding comparable power conversion efficiencies of 11.374%. The findings of this study can serve as valuable insights for the design of more advanced and efficient perovskite solar cells based on mineral perovskite layers.

## Introduction

The demand for clean energy in both domestic and industrial sectors has emerged as a highly significant concern for the fields of technology and science, which concurrently grapple with environmental considerations. With projections indicating a forthcoming surge in global energy consumption and the realization that traditional energy sources like coal and oil will fall short in meeting humanity's needs, it becomes imperative to reassess our energy supply strategies in order to harness the pure energies available in the universe [1]. An effective solution lies in harnessing the abundant thermal and light energy from the sun. This renewable resource, readily available to us at no cost, holds immense potential as it generates an astonishing energy with  $1.5 \times 10^{18}$  kWh/year of radiation providing approximately more than 100 times of entire fossil resources [1]. In 1953, researchers pioneered the conversion of solar energy into electricity by utilizing silicon material to develop the first-generation solar cells [2]. However, the cost of pure silicon for industrial applications is prohibitively high. In response, scientists developed photovoltaic technology, enabling the utilization of solar

energy while reducing production and construction costs. Subsequently, the field of photovoltaic technology witnessed the advent of successive generations of solar cells, each with distinct advantages and limitations [3–6]. Since 2014, there has been a growing interest in perovskite solar cells (PSCs) within the scientific community due to their remarkable efficiency advancements compared to previous generations. Over the past decade, the efficiency of PSCs has increased from 3.8% to 25.5% [5–7]. These cells utilize perovskite materials, which are abundant in nature and possess favorable properties such as a direct band gap, low exciton binding energy, few crystal defects, balanced electron-hole transfer, high charge mobility, low production costs, and high efficiency [8–11]. However, PSCs still face challenges related to temperature and humidity sensitivity [12,13]. Numerous perovskite compositions share similar structural characteristics. Fig. 1 illustrates the structure of a cubic perovskite unit cell, representing well-known materials for PSCs, such as MAPbI<sub>3</sub>, FAPbI<sub>3</sub>, and CsSnI<sub>3</sub> [14,15]. These materials have an ABX<sub>3</sub> composition, highlighting their cubic perovskite unit cell structure.

Organic-inorganic PSCs, particularly MAPbI<sub>3</sub>, have been extensively

\* Corresponding author.

E-mail address: [aashokri@alzahra.ac.ir](mailto:aashokri@alzahra.ac.ir) (A. Shokri).

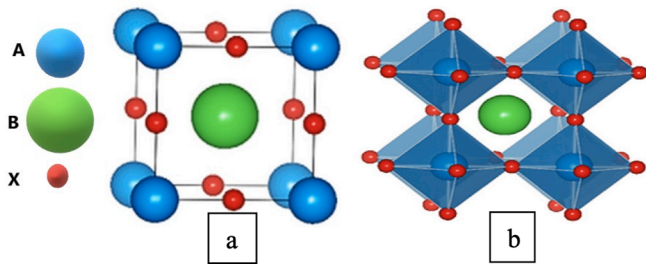


**Fig. 1.** The ideal cubic perovskite unit cell. (a) A-cations (blue) occupy the lattice corners, B- cations (green) occupy the interstitial site, and X anions (red) occupy lattice faces. (b) An alternative view depicting B cations assembled around X anions to form  $BX_6$  octahedra, as BX bonds are responsible for determining electrical properties [16]. (For interpretation of the references to colour in this figure legend, the reader is referred to the web version of this article.)

investigated in the scientific literature. A multitude of studies have proposed diverse designs and methodologies aimed at optimizing the efficiency of organic–inorganic PSCs structures. Researchers, for instance, have delved into light-trapping techniques within PSCs, employing plasmonic core/shell nanorod arrays, including materials such as Au and Ag. This exploration extends to textured HTM-free perovskite/PbS Quantum Dot solar cells [17–19]. Furthermore, endeavors to enhance the efficiency of PSCs encompass investigations into the impact of the location and size of plasmonic nanoparticles, such as Ag and Au. Additionally, the incorporation of random plasmonic nanoparticles is also a subject of study [20,21]. Another notable advancement involves the enhancement of the efficiency of half-tandem CIGS/PSCs through the strategic design of a nano-prism nanostructure for controllable light trapping, resulting in an increased efficiency of up to 19.29% [22]. Furthermore, the scientific community has suggested the utilization of a variety of materials for hole transport layers, including polymers, organic compounds, and single-walled carbon nanotubes [23–27]. It is important to emphasize that ongoing research is actively exploring diverse avenues to achieve optimal performance for PSCs based on organic–inorganic light-absorbing materials [27–29]. However, they suffer from certain limitations, including intrinsic instability and susceptibility to temperature and photochemical degradation of organic components [30–32]. To address these drawbacks, researchers have explored the use of inorganic cations such as K, Rb, and Cs in perovskite unit cells to develop all-inorganic PSCs with enhanced optoelectronic performance and stability [33–35]. Notably, the substitution of organic cations with minerals like Cs has significantly boosted the efficiency of mineral PSCs from 2.9% to 20.8% over the past six years [36–38]. Thermal calorimetric analyses have revealed that organic cation-based perovskites undergo decomposition at temperatures below 125 °C, whereas inorganic cation-based perovskites exhibit decomposition at temperatures exceeding 500 °C [34,39]. Moreover, in contrast to organic materials, most perovskite minerals exhibit superior resistance to humidity and enhanced stability under high temperature and light conditions [40–42]. Despite these advancements, there is still considerable room for further progress in exploring diverse perovskite structures to achieve solar cells with optimized performance. In this study, we examine four configurations of PSCs with varying layers of electron transporters, hole transporters, and metal electrodes for electron collection. The focus is on investigating the effectiveness of  $RbGeBr_3$ , a mineral as the active layer responsible for light absorption. The charge density and current continuity equations, commonly used in semiconductor studies, are solved for these structures. Four pivotal factors are meticulously compared and evaluated across distinct architectures: the short-circuit current ( $J_{sc}$ ), the open circuit voltage ( $V_{oc}$ ), the fill factor (FF), and the PCE.

This article is structured as follows: The second section provides an overview of the design and overall performance of the PSCs electrostatic

structure. Subsequently, the third section discusses the general computational method, presenting an overview of the research and model techniques employed. The fourth section details the simulation steps. The fifth section exhibits the results and discussions; showcasing the outputs and diagrams of the four structures by considering the impact of temperature and thickness variations on the results. The sixth section presents the conclusion derived from the study and finally, the seventh section discusses the feasibility of the work. The findings of this research offer valuable insights for the development of PSCs based on minerals with more complex structures and higher efficiency.

### Structure design method of PSCs with $RbGeBr_3$ inorganic active layer

Ongoing extensive research endeavors are dedicated to enhancing the efficiency of organic–inorganic PSCs [28,29,43]. Simultaneously, considerable scientific attention has been directed towards inorganic perovskite materials, as depicted in Fig. 2, owing to their significant physical characteristics. Examples of such inorganic perovskite materials include  $AVO_3$ ,  $Cs_2BiAgI_6$ ,  $TiGeX_3$ , and others [44–47]. Currently, there is significant potential for research in the field of all-mineral solar cells due to the limited amount of existing research in this area. Recent studies focusing on the impact of Cs in structural perovskite in PSCs have yielded various compounds and structures with efficiency ranging from 2.9% to 20.8%, such as some research on  $CsSnI_3$ ,  $CsPbI_3$ , [28,38,42,48].

In brief, research into all-mineral PSCs commenced in 2015 when Kolbak and colleagues introduced inorganic PSCs containing  $CsPbX_3$  materials, such as  $CsPbBr_3$ ,  $CsPbI_3$ , and  $CsPbCl_3$  [49,50]. They conducted a direct comparison between the organic–inorganic perovskite  $MAPbBr_3$  and the all-inorganic perovskite  $CsPbBr_3$ , enabling the identification of crucial differences in their structural, thermal, and electronic properties [49]. To ensure a fair comparison between devices made from these materials, both were fabricated similarly on mesoporous titanite frameworks. While both materials exhibited a direct band gap,  $CsPbBr_3$  demonstrated greater temperature stability compared to its organic counterpart. Furthermore, an analysis of the results confirmed that cesium-based devices exhibited efficiency on par with methylammonium-based devices. Fig. 3 illustrates that, even after two weeks of exposure to dry air (approximately 15% - 20% humidity), continuous intense light exposure (at maximum power), and electron beam irradiation, Cs-based solar cells displayed superior stability compared to methylammonium-based solar cells [34].

Efforts aimed at improving the efficiency of inorganic PSCs and advancing the understanding of these materials as electronic components continued until 2016. A pivotal development occurred when Lin-Jer Chen and his team introduced a significant breakthrough [36]. They reported the creation of PSCs based on cesium with tin replacing lead in

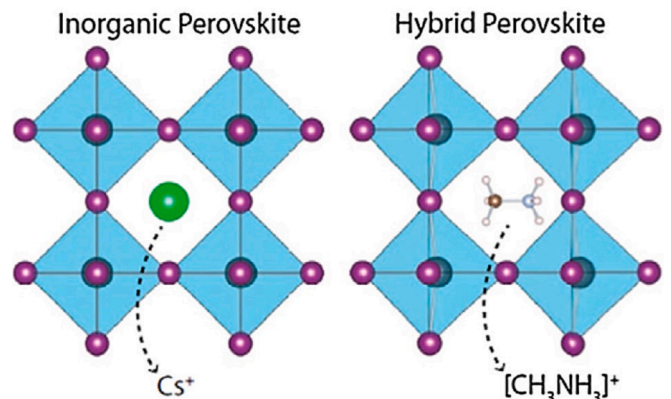


**Fig. 2.** Spherically symmetric inorganic cesium ( $Cs^+$ ) cation replaced instead of the non-spherically symmetric organic methylammonium ( $[CH_3NH_3]^+$ ) [16].

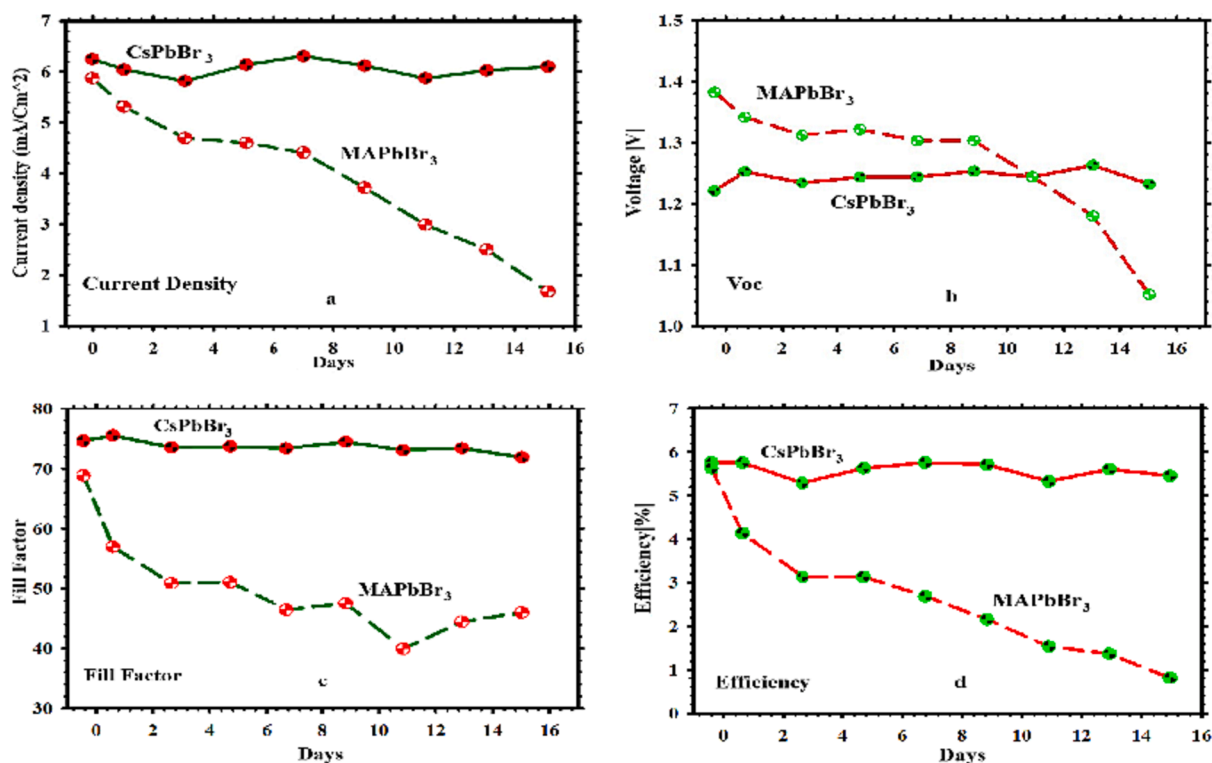


Fig. 3. Obtaining analysis of MAPbBr<sub>3</sub> and CsPbBr<sub>3</sub> cells. Figures illustrate the cell parameters, a) J<sub>SC</sub>, b) V<sub>OC</sub>, c) Fill factor, and d) efficiency, as a function of time, demonstrating the much greater stability of CsPbBr<sub>3</sub>-based cells with aging. Redrawn with modification from [34].

an all-inorganic perovskite structure. This breakthrough involved the experimental examination of three distinct all-inorganic CsSnX<sub>3</sub> solar cells (CsSnI<sub>3</sub>, CsSnBr<sub>3</sub>, CsSnCl<sub>3</sub>) within the ITO/TiO<sub>2</sub>/CsSnX<sub>3</sub>/HTM/Au framework [36]. Among these cells, the highest efficiency of 12.96% was achieved by the CsSnI<sub>3</sub> solar cell when subjected to 1.5 AM radiation. Fig. 4a and 4b illustrate the voltage-current characteristics of all three cells and compare the efficiency of the CsSnI<sub>3</sub> inorganic PSCs with that of the organic PSCs, MAPbI<sub>3</sub>, over a span of 17 days. Notably, it is evident that the efficiency of the CsSnI<sub>3</sub> cell experienced a less pronounced decrease compared to the efficiency of MAPbI<sub>3</sub> [36]. In subsequent years, persistent efforts were dedicated to enhancing the efficiency of this particular cell, ultimately achieving a notable 19% efficiency rate in 2019 [51,52]. Similar to hybrid perovskites, CsPbX<sub>3</sub> perovskites can be readily produced through solution-based processes and have demonstrated optoelectronic properties akin to their organic counterparts [53–55].

In 2021, Hailian Wang and his research team delved into the development process of CsPbX<sub>3</sub> perovskites through molecular engineering methods, conducting a comprehensive comparison with MAPbI<sub>3</sub> organic perovskite cells [7]. They scrutinized various aspects, including differences in molecular structure, the malleability of two-dimensional structures, and surface and interface modifications. For instance, their research conclusively demonstrated that inorganic perovskites exhibit significantly higher stability at elevated temperatures when compared to organic perovskites such as MAPbI<sub>3</sub>, as depicted in Fig. 5 [7].

However, there has been little investigation conducted on the inorganic perovskite materials specially elements, Rb and K within the first group [56–59]. According to the aforementioned explanations, the primary objective of this research was to scrutinize the light-absorbing properties of the mineral RbGeBr<sub>3</sub> in four distinct PSC configurations. The crystal structure of this compound, RbGeBr<sub>3</sub>, closely resembles a perovskite cubic unit cell, as depicted in Fig. 6. The halide perovskite is characterized by the ABX<sub>3</sub> structure, where A represents an alkali metal (A = K, Rb, Cs), B signifies a metalloid (in this case, Germanium, chosen due to the superior optical absorption and optical conductivity of Ge-

based compounds compared to Pb-based compounds [59]), and X denotes a halogen (X = F, Cl, and Br). In this cubic structure, the atomic positions of A, B (as cations), and X (halogen) atoms in ABX<sub>3</sub> are precisely defined as follows: A at (0, 0, 0), B at (0.5, 0.5, 0.5), and X at (0.5, 0.5, 0), as illustrated in Fig. 6. The inorganic halide perovskite demonstrates semiconducting behavior with a direct band gap in its cubic phase [60].

Fig. 7 reveals that this substance possesses a direct band gap of 1.49 eV, making it well-suited as a light-absorbing layer with advantageous optical properties within the visible light spectrum. Additionally, the effective masses of holes and electrons are denoted as  $m_h^*$  and  $m_e^*$ . In the crystal lattice of this material, the lattice base vectors a, b, and c are mutually perpendicular, and the x, y, and z directions align with [100], [010], and [001], respectively. For instance, at the [100] plane in the case of RbGeBr<sub>3</sub>, the effective electron mass measures 1.31, while the effective hole mass is 0.18 when compared to the mass of a stationary electron in the x-direction [60]. These values play a crucial role in influencing the mobility of electrons and holes [60].

The general working principle of PSCs is shown in Fig. 8, which presents an overview of the electrostatic structure of a PSCs, comprising multiple layers composed of different materials.

The initial layer, known as the transparent electrode (TCO), consists of a wide band gap, enabling easy penetration of sunlight into the cell [52]. Upon traversing the transparent layer, the solar spectrum enters the active layer, which encompasses two sub-layers: the light absorber layer and the Electron Transfer Layer (ETL). These sub-layers are fabricated using semiconductor materials possessing distinct band gaps, allowing a broad range of light to pass through and get absorbed. The absorber layer absorbs the incident light, generating free charge carriers that subsequently migrate towards the electron-conducting layers. Electrons transit from the lowest unoccupied molecular orbital (LUMO) of the absorber layer to the lowest unoccupied molecular orbital (LUMO) of the ETL, while holes form from the highest occupied molecular orbital (HOMO) of the light-absorbing layer move to the highest

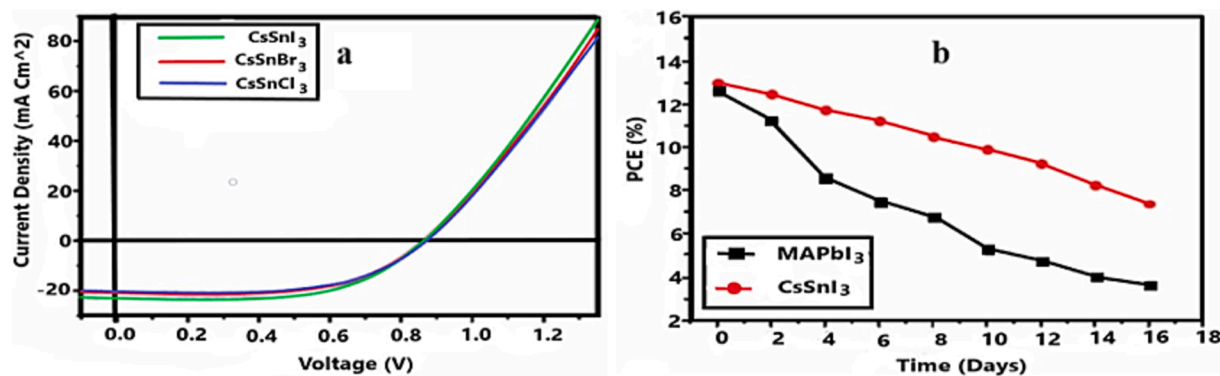


Fig. 4. a) J-V characteristics of  $\text{CsSnI}_3$ ,  $\text{CsSnBr}_3$  and  $\text{CsSnCl}_3$  solar cells, b) efficiency, for the reference and  $\text{CsSnI}_3$  quantum rod-based devices. redrawn with modification from [36].

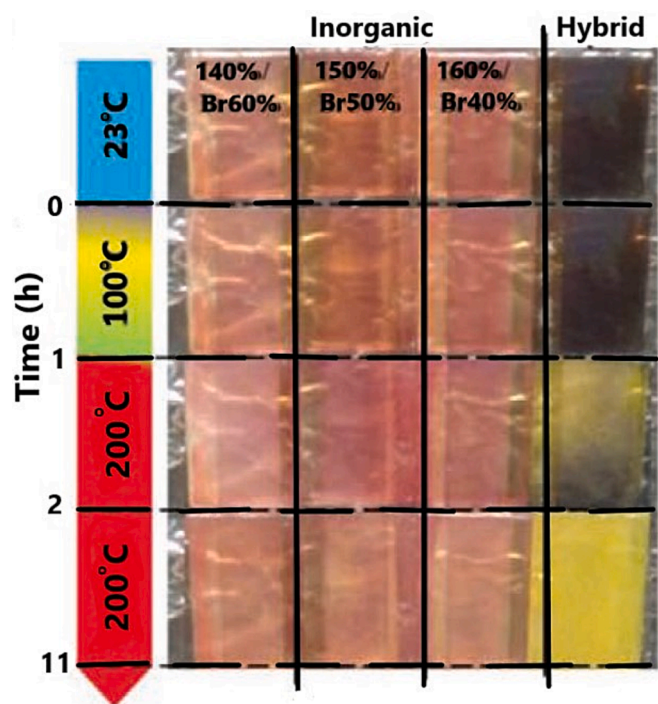


Fig. 5. Photographs of inorganic and hybrid (organic/inorganic) perovskite films annealed at different temperatures under dry condition [55].

occupied molecular orbital of the subsequent layer, which further transitions to the Hole Transporting Layer (HTL). Ultimately, these charge carriers are collected by electrodes, typically composed of metals like gold, silver, or graphene. Moreover, through density function theory (DFT) calculations, the primary electronic and optical characteristics of  $\text{RbGeBr}_3$  have been determined [56,59,60]. In this study, four planar structures incorporating inorganic perovskite as the light-absorbing material were examined as inorganic PSCs. The design of these structures involved the careful selection of materials for different layers and the sequencing of their placement. This selection was guided by a thorough investigation and review of reputable sources, including counterparts in the realm of organic-mineral solar cells [35,38]. The objective of this research was to explore the behavior of the  $\text{RbGeBr}_3$  mineral perovskite material within a solar cell context, comparing it to its counterparts—specifically, cesium-based mineral PSCs that have been studied both experimentally and theoretically [35,36]. Notably, the role of  $\text{RbGeBr}_3$  as an inorganic material in a solar cell has not been investigated either experimentally or theoretically, and this study aims to fill this gap in understanding. In this investigation, all various

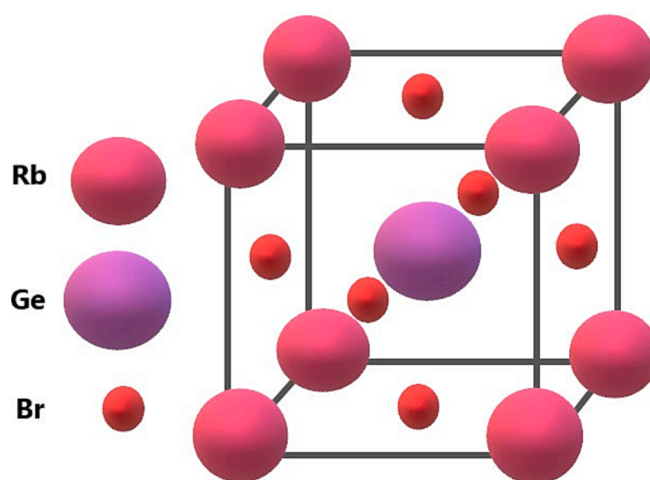


Fig. 6. Crystal structure of cubic halide perovskites  $\text{ABX}_3$  ( $A = \text{Rb}$ ;  $X = \text{Br}$ ). Redrawn with modification from [56].

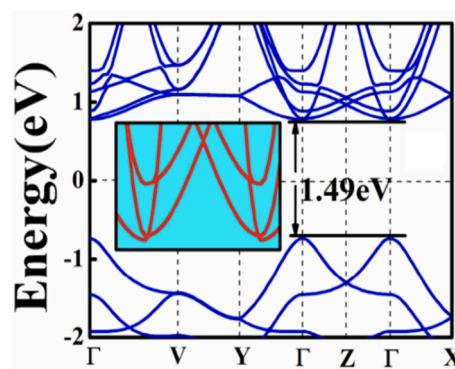


Fig. 7.  $\text{RbGeBr}_3$  possesses a direct band gap of 1.49 eV [60].

structures have the same structure as shown in Fig. 8. The first and second structures of the four PSCs, with the ETL comprising the semiconductor material  $\text{TiO}_2$  and the HTL comprising the organic material  $\text{P}_3\text{HT}$  [36,61–63]. However, in the first structure, the electron-conducting electrode has been replaced with gold (Au), while in the second structure, silver (Ag) serves as the replacement. The third and fourth structures feature the ITO semiconductor material for the ETL and the PEDOT:PSS semiconductor material for the HTL, along with Au and Ag metal electrodes [64–66]. The desired sequence of multilayers for this research listed below from the first desired structure to the fourth

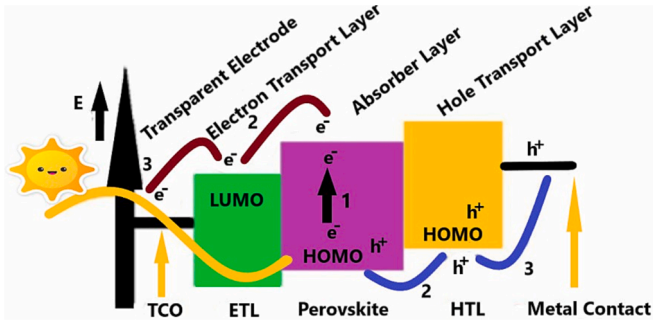


Fig. 8. The electrostatic structure of a PSCs overall performance. Redrawn with modification from [13].

and last structure:

- I. FTO/<sup>1</sup>TiO<sub>2</sub>/RbGeBr<sub>3</sub>/<sup>2</sup>P<sub>3</sub>HT/Au
- II. FTO/TiO<sub>2</sub>/RbGeBr<sub>3</sub>/P<sub>3</sub>HT/Ag
- III. FTO/ITO//RbGeBr<sub>3</sub>/<sup>3</sup>PEDOT:PSS/Au
- IV. FTO/ITO/<sup>4</sup>RbGeBr<sub>3</sub>/PEDOT:PSS/Ag

Table 1, presents the necessary parameters for the simulation, including the conduction band density  $N_c$ , valence band density  $N_v$ , electron donor density  $N_d$ , and electron acceptor density  $N_a$ . Furthermore, the table provides data regarding electron affinity ( $\chi$ ), which signifies the energy acquired when an electron is relocated from the vacuum region just outside the semiconductor to the base of the conduction band within the semiconductor. It also includes information on band gap energy  $E_g$ , which denotes the energy differential between the uppermost point of the valence band and the lowermost point of the conduction band in semiconductors and insulators. In addition, the table presents the dielectric constant  $\epsilon_r$ , a parameter gauging a substance's capacity to store electrical energy within an electric field and electron defect density  $N_t$  in form of Gaussian distribution. Additionally, this expression furnishes the electron mobility  $\mu_e$  and hole mobility  $\mu_h$  values. Electron mobility signifies the speed at which an electron can traverse a metal or semiconductor under the influence of an electric field, and there is a corresponding parameter for holes known as hole mobility. Furthermore, the expression denotes the lifetimes of electrons  $\tau_e$  and holes  $\tau_h$ .

### General computational method

In this section, we present the results pertaining to various types of PSC structures, utilizing an optoelectronic model grounded in semiconductor physics research and employing the finite element method through COMSOL simulation. To comprehend how the target material responds to incident light radiation, the following equations within the optoelectronic model must be employed. The initial step involves determining the absorption coefficient  $\alpha(\omega)$ , which can be derived from the Equation (1) presented below [56]:

$$\alpha(\omega) = \frac{2\pi\omega\sqrt{-\text{Re}(\omega) + |\epsilon|}}{c\sqrt{2}} \quad (1)$$

In this particular context, the symbol denotes the permeability constant  $|\epsilon|$  of the material medium, the frequency ( $\omega$ ) of the radiant light spectrum, and the speed of light  $c$ . The absorption coefficients of perovskite materials for solar spectrum typically to be within the range of  $10^5$  [cm<sup>-1</sup>]

<sup>1</sup>]. To determine the penetration depth, which is the reciprocal of the absorption coefficient, careful attention must be paid to the material's absorption coefficient. This calculation enables the determination of the minimum thickness in nanometers necessary for optimal light absorption. Equation (2) represents the comprehensive refractive index of the material, comprising the real refractive index  $n(\omega)$ , responsible for light reflection from the material, and the imaginary refractive index  $k(\omega)$ , crucial in solar cell simulations as it governs the absorption of the sun-light spectrum within the material [56].

$$N(\omega) = n(\omega) + ik(\omega) \quad (2)$$

The amount of light reflection from the cell is quantified by the reflection coefficient  $R(\omega)$  [51,62]:

$$R(\omega) = \frac{(n-1)^2 + k^2}{(n+1)^2 + k^2} \quad (3)$$

Finally, the material's optical conductivity  $\sigma(\omega)$  is shown [56]:

$$\sigma(\omega) = -\frac{i\omega}{4\pi} \epsilon(\omega) \quad (4)$$

Semiconductor equations were used to study the electrical behavior of the solar cell; mainly the current density–voltage (J-V) characteristics are considered. The equations used in the model are Poisson, transport, and continuity equations. The Poisson equation is given by Equation (5) [67,68]:

$$\nabla \cdot (-\epsilon_0 \epsilon_r \nabla V) = \rho \quad (5)$$

where  $\epsilon_0$  is the constant of vacuum permeability and potential gradient  $\nabla V$ , and  $\epsilon_r$  is the material's dielectric coefficient. To get the passing charge density, it is presented in Equation (6) [67,68]:

$$\rho = q(p - n + N_d^+ - N_a^-) \quad (6)$$

where  $q$  is the electronic charge,  $p$  is the density of holes,  $n$  is the density of electrons,  $N_d^+$  is the impurity density of electrons ionized in the system by the substance that donates electrons (also known as ETL), and  $N_a^-$  shows the impurity density of ionized electrons in the system by the electron acceptor material that acts as a light absorber and HTL. Equation (7) can be used to determine the density of holes and electrons:

$$n = N_c e^{-\frac{E_c - E_F}{K_B T}} \quad p = N_v e^{-\frac{E_v - E_F}{K_B T}} \quad (7)$$

The Fermi energy ( $E_F$ ) of the selected material under is an important parameter, while the Boltzmann constant  $K_B$  at the solar cell temperature, typically 300 K, plays a significant role. Additionally,  $E_c$  and  $E_v$  represent the energies associated with the conduction band and valence band, respectively. Based on the Equation (7), the conduction band energy is represented by  $E_c = -(V + \chi_0)$ , where it is lower than the vacuum voltage  $V$  by an amount proportional to the electron affinity energy  $\chi_0$ , and the valence band energy is represented by  $E_v = -(V + \chi_0 + E_{g0})$ . Furthermore, the density of effective states in the conduction band and the valence band is determined using the following expressions:

$$N_c = 2 \left( \frac{2\pi m_n^* K_B T}{h^2} \right)^{3/2} \quad (8)$$

$$N_v = 2 \left( \frac{2\pi m_p^* K_B T}{h^2} \right)^{3/2} \quad (9)$$

The continuity equation is given by Equation (10) and Equation (11) [67]:

<sup>1</sup> Titanium dioxide.

<sup>2</sup> Poly(3-hexylthiophen-2,5-diyl).

<sup>3</sup> Poly(3,4-ethylenedioxythiophene) polystyrene sulfonate.

<sup>4</sup> Rubidium-triboromide-germanates.

**Table 1**

The physical characteristics of the layer materials used in PSCs.

	ETL	ETL	Absorber layer	HTL	HTL
Parameters	TiO <sub>2</sub> [61,62]	ITO [64,65]	RbGeBr <sub>3</sub>	P <sub>3</sub> HT [63,72]	PEDOT: PSS [64,66]
Thickness of layer(nm)	80	80	200	300	300
$\chi$ (eV)	4.00	4.80	3.80	3.10	2.90
$E_g$ (eV)	3.20	3.65	1.49 [60]	1.85	2.20
$\epsilon_r$	9.00	8.90	7.00	3.40	3.00
$N_c$ (cm <sup>-3</sup> )	10 <sup>19</sup>	10 <sup>18</sup>	3.7 × 10 <sup>19</sup> [60]	10 <sup>22</sup>	2.2 × 10 <sup>15</sup>
$N_v$ (cm <sup>-3</sup> )	10 <sup>19</sup>	10 <sup>18</sup>	2.1 × 10 <sup>18</sup> [60]	10 <sup>22</sup>	1.8 × 10 <sup>18</sup>
$N_a$ (cm <sup>-3</sup> )	-	-	2.0 × 10 <sup>13</sup>	3.7 × 10 <sup>18</sup>	3.7 × 10 <sup>14</sup>
$N_d$ (cm <sup>-3</sup> )	5 × 10 <sup>19</sup>	10 <sup>20</sup>	-	-	-
$\mu_e$ (cm <sup>2</sup> /V.s)	0.02	10	8.5 × 10 <sup>2</sup>	2 × 10 <sup>-4</sup>	2 × 10 <sup>-2</sup>
$\mu_h$ (cm <sup>2</sup> /V.s)	2	10	8.5 × 10 <sup>2</sup>	2 × 10 <sup>-4</sup>	2 × 10 <sup>-4</sup>
$\tau_e, \tau_h$ (ns)	5, 2	5, 2	2, 2	0.1, 0.1	0.1, 0.1

$$\frac{\partial n}{\partial t} = \frac{1}{q} \nabla \cdot \mathbf{J}_n - U_n + G_n \quad (10)$$

$$\frac{\partial p}{\partial t} = \frac{1}{q} \nabla \cdot \mathbf{J}_p - U_p + G_p \quad (11)$$

where  $U_n$  is the recombination rate for the electrons,  $U_p$  is the recombination rate for the holes,  $G_n$  is the generation rate for electrons, and  $G_p$  is the generation rate for holes. The transport equation is given by Equation (12) and Equation (13) [67]:

$$\vec{J}_n = -qn\mu_n \nabla \phi + qD_n \nabla n \quad (12)$$

$$\vec{J}_p = -qp\mu_p \nabla \phi + qD_p \nabla p \quad (13)$$

where  $J_n$  is the current density for the electrons,  $J_p$  is the current density for the holes,  $D_n$  is the diffusion coefficient for electrons,  $D_p$  is the diffusion coefficient for holes,  $\mu_n$  is the electron mobility and  $\mu_p$  is the hole mobility. The diffusion length relates to the charge carrier lifetime and diffusion coefficient according to Equation (14):

$$L_{n,p} = \sqrt{D_{n,p} \tau_{n,p}} \quad (14)$$

After considering the factors mentioned and solving the continuity equations in a semiconductor while accounting for the optical properties of materials utilized in PSCs, the following equations are derived to yield the conclusive results of cell simulation [69]:

$$I = I_{ph} - I_D = I_{ph} - I_0 \left[ \exp \left[ \frac{eV}{K_B T_c} \right] - 1 \right] \quad (15)$$

The difference between the photon current,  $I_{ph}$ , and the ideal current of the diode,  $I_D$ , is the net current  $I$ . The dark saturation current,  $I_0$ , is highly dependent on temperature. Equation (16) provides evidence for the significant influence of the amount of light absorbed by the solar cell and the external voltage applied on the generated current. When the voltage within the cell is reduced to zero, the current density, known as the short circuit current density ( $J_{sc}$ ), reaches its peak value, resembling a short circuit condition. Conversely, the voltage attains its maximum point, termed the open circuit voltage, when no current flows through the solar cell, resembling an open circuit situation [69]:

$$V_{oc} = \left( \frac{K_B T}{q} \right) \ln \left( \frac{J_{sc}}{J_0} \right) \quad (16)$$

The term  $J_0$  represents the difference between the current density influenced by the applied voltage in the system and the current density in the absence of voltage. In this context, the output power of the solar cell can be obtained by multiplying the maximum current and the maximum voltage generated within the cell [69]:

$$P_{max} = I_{max} V_{max} \quad (17)$$

The equation  $I_{max} = \frac{eV_{max}}{K_B T_c + eV_{max}} (I_{sc} + I_D)$  yields the highest achievable electric current. With these factors taken into account, the equation shown below can be used to determine the cell's [57]:

$$\eta = \frac{P_{max}}{P_{in}} = \frac{I_{max} V_{max}}{P_{in}} \quad (18)$$

$P_{in}$  is the light input power, which in each PSC is equivalent to 100 mW/cm<sup>2</sup>.

Furthermore, it is imperative to acknowledge that semiconductor materials undergo changes in their electrical properties as a consequence of temperature variations. Consequently, the electrical characteristics of PSCs exhibit variability under the influence of temperature. Notably, the open circuit voltage of the solar cell is predominantly affected by temperature, while the impact on the short circuit current density remains minimal. The following equations elucidate the temperature's influence on voltage [70]:

$$V_{oc} = \frac{KT}{q} \left( \ln J_{sc} - \ln \left[ BT^3 \exp \left( -\frac{V_g(T)}{V_t} \right) \right] \right) \quad (19)$$

In the given equation,  $B$  is a constant independent of time. Two parameters are explicitly defined: the thermal voltage denoted as  $V_t = \frac{KT}{q}$ , where  $k$  is the Boltzmann constant,  $T$  is the temperature, and  $q$  is the elementary charge; and the energy gap voltage denoted as  $V_t = \frac{E_g}{q}$ , where  $E_g$  is the energy gap. To assess the impact of temperature on the open circuit voltage, it is advisable to derive the equation  $\frac{dV_{oc}}{dT}$  [70]:

$$\frac{dV_{oc}}{dT} = -\frac{(V_{g0} - V_{oc}) + 3V_T}{T} + V_T \left( \frac{1}{J_{sc}} \frac{dJ_{sc}}{dT} + \frac{1}{V_T} \frac{dV_g}{dT} \right) \quad (20)$$

In the given equation, the first term predominates over the second term, rendering its omission justifiable. Consequently, it is evident that an increase in temperature results in a decrease in the open circuit voltage of a PSCs.

### Simulation details

This section has provided an elucidation of the simulation steps, encompassing the utilization of the module, specification of boundary conditions, simulation of the solar radiation spectrum, mesh utilization, and the correlation between the absorption coefficient and carrier production rate, as per the aforementioned equations.

In this investigation, the COMSOL simulator employs the semiconductor module in a two-dimensional context. As previously outlined, semiconductor equations are employed to scrutinize the electrical behavior of the solar cell. The primary focus involves the determination

of the generation rate within the PSCs, followed by an examination of the current density–voltage (J-V) characteristics. The model incorporates several fundamental equations, namely the Poisson equation and the continuity and transport equations (Equations (5), (10)–(13), respectively). Furthermore, the semiconductor module integrates a set of boundary conditions. Specifically, the boundaries in contact with insulators are subject to zero load boundary conditions, while for boundaries distant from the active area, the electric current  $J_n$  and  $J_p$  are zero. These boundary conditions are precisely defined through Neumann boundary conditions, expressed as  $\hat{n} \cdot J_n = 0$  and  $\hat{n} \cdot J_p = 0$  [71].

Furthermore, concerning the output terminals, the boundary conditions contingent on current are entirely determined by the specific type of metal–semiconductor connection and the module utilized.

Table 1 presents the essential electrical simulation parameters corresponding to various layers proposed for PSCs, encompassing electron-transporting (ETL) and hole-transporting (HTL) layers. In addition to these parameters, optical properties play a crucial role, particularly the refractive index and its inherent characteristics, as described in Equation (2). When light traverses a non-transparent material, a portion is absorbed upon striking the substance, while the remainder follows the Beer-Lambert law. The absorbed light is determined by the imaginary part of the refractive index  $k(\omega)$ , establishing a direct relationship with the absorption coefficient of the material. In the COMSOL simulator, the refractive indices of materials, sourced from reliable references, are employed as interpolation functions. Specifically, the materials include  $\text{TiO}_2$  [73], ITO [57], PEDOT:PSS [74],  $\text{P}_3\text{HT}$  [63], Au [75], Ag [75], FTO [73], and  $\text{RbGeBr}_3$  [56]. In the calculation of carrier generation rate in a solar cell, careful consideration is given to the absorption coefficient of the material—an intrinsic property of the medium—defined by the equation  $\alpha(\lambda) = \frac{4\pi k(\lambda)}{\lambda}$  (or Equation (1), as previously mentioned). This absorption coefficient is pivotal in assessing the impact of the material on incident radiation, particularly the 1.5 AM solar spectrum. The structure designed for this purpose is illustrated in Fig. 9, mirroring the functionality depicted in Fig. 8. The presented design demonstrates the ingress of radiation from the 1.5 AM solar spectrum into the solar cell through the FTO layer. Notably, this FTO layer is situated above the ETL, facilitating the subsequent progression of the radiation to reach the light-absorbing layer.

The generation rate of carriers is calculated through the following Equation (21):

$$G(x, \lambda) = \frac{4\pi}{hc} \int_{\lambda_1}^{\lambda_2} k(\lambda) \Phi(\lambda) \exp(-\alpha(\lambda)x) d\lambda \quad (21)$$

Here  $\Phi(\lambda)$  represents the solar spectrum, utilized in COMSOL as an interpolation function. The incident wavelength range is specified with  $\lambda_1$  at 300 nm and  $\lambda_2$  at 800 nm. It's noteworthy that this wavelength range is chosen based on the band gap of the investigated perovskite material  $\text{RbGeBr}_3$ , which is 1.49 eV, and its extinction coefficient reaches zero at 800 nm. The absorption coefficient  $\text{RbGeBr}_3$  material are shown in Fig. 10 [56].

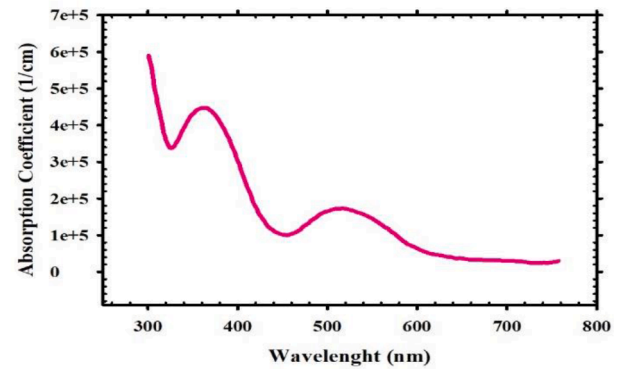


Fig. 10. The absorption coefficient rb material. Redraw figure from [56].

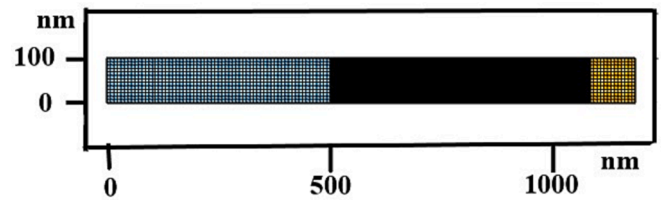


Fig. 11. Illustrates two-dimensional meshing in desired structure.

In the subsequent stage, the COMSOL software employs finite element methods (FEM) to solve equations within simulation modules. This involves dividing the modeled shape into small elements, known as a mesh. The chosen meshing method for these specific architectures is the Mapped method. It is crucial to highlight that a greater number and finer mesh size in the structures contribute to more accurate calculated results. Fig. 11 illustrates the two-dimensional meshing in the desired structure. Notably, the perovskite area, serving as the light-absorbing layer, necessitates a particularly fine mesh to enhance the precision of the calculations.

### Discussions and results

The primary objective of this paper is to select the most efficient and optimal structure among the four given structural options in section 2, in order to achieve the highest efficiency. Additionally, the PCE of these structures is being analyzed in relation to variations in temperature while operating at their respective highest efficiency levels. To determine the maximum PCE of the PSCs, the thickness of the HTL is set at 300 nm. However, the thickness of the light-absorbing mineral layer ( $\text{RbGeBr}_3$ ) is varied from 200 to 500 nm, and the thickness of the ETL is varied from 80 to 110 nm. In addition, when the calculation was done, the graphs are plotted in two scenarios in this study: (i), the thickness of absorber layer is changed from 200 nm to 500 nm when the ETL keep constant at 80 nm, and (ii), when the ETL is varied from 80 nm to 110 nm while the thickness of absorber layer remain stable at 200 nm. Furthermore, the four key parameters of the solar cell, namely  $J_{sc}$ ,  $V_{oc}$ , FF, and PCE, have been calculated to compare the performance and PCE of the best structure. Graphs illustrating the results of these calculations are provided for each structure. Moreover, the current density – voltage (J-V) and output power- voltage (P-V) are plotted for one of simulations which is depicted the higher efficiency than the other states; that It was done for all distinct structures. should be noted that this study assumes a penetration length of 100 nm for both electrons and holes based on [7].

- I. FTO/ $\text{TiO}_2$ / $\text{RbGeBr}_3$ / $\text{P}_3\text{HT}$ /Au,
- a. T = 300 K

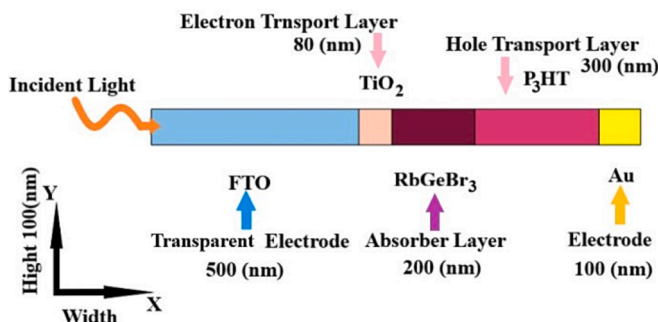


Fig. 9. The design of the desired structure.



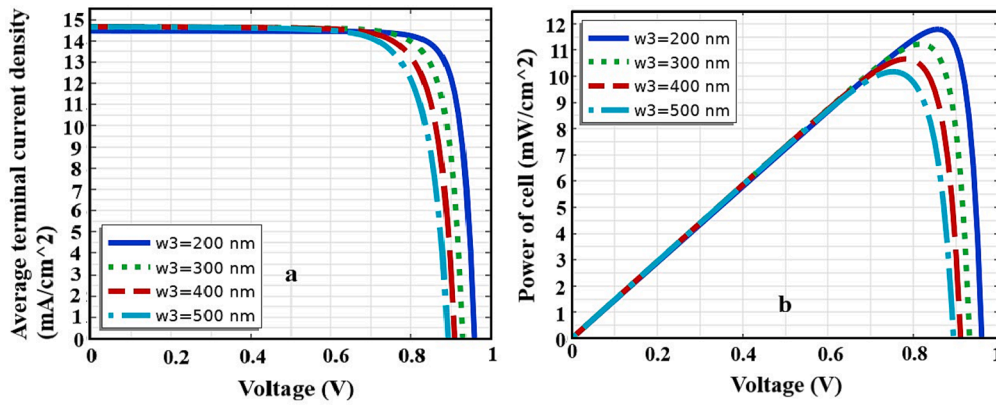


Fig. 12. a) The current–voltage (J-V), b) Power of cell (P-V) at 300 K.

The ETL of the first structure is TiO<sub>2</sub>, the HTL is P<sub>3</sub>HT, and the electron-collecting metal electrode is Au. In accordance with the results at a constant temperature of 300 K, in Fig. 12a, it shows the average terminal current density- voltage is increasing slightly. While, Fig. 12b, output power-voltage illustrates decreasing gradually. In Fig. 12, the thickness of the TiO<sub>2</sub> as the ETL is maintained at 80 nm. However, the thickness of the light absorber layer is increased from 200 nm to 500 nm. Considering the case where the light-absorbing layer is 200 nm thick, the short-circuit current density of the solar cell in Fig. 12a, is found to be 14.47 mA/cm<sup>2</sup>, which is highly dependent on the incident light radiation and its absorption by the absorber layer.

In this scenario, the solar cell behaves as a short circuit, resulting in the highest level of generated current. The open circuit voltage is approximately 0.96 V, representing the highest voltage achieved when no current flows through the cell due to an open circuit configuration as shown in Fig. 12a. Moreover, the output power of the PSCs is zero in

both the short circuit and open circuit conditions. The solar cell reaches its maximum power, which is the product of the maximum current and maximum voltage, when it operates under positive voltage with parallel and series resistors, analogous to an optical component. Therefore, in Fig. 12b, the graphs are illustrated the electric power generated by the cell exhibits a gradually decline ranging from 1 mW/cm<sup>2</sup> to 2 mW/cm<sup>2</sup>.

In the first scenario, the thickness of the absorber layer increases from 200 nm to 500 nm while the ETL remains unchanged at 80 nm; Fig. 13 illustrates the variation of solar cell parameters with the thickness of the absorber layer. As shown in Fig. 13a and 13b respectively, the short-circuit current slightly increases by 0.02 mA/cm<sup>2</sup>, while the open circuit voltage experiences a negligible decrease. In these cases, the fill factor decreases by approximately 0.2 (Fig. 13c). The final PCE in this case is calculated as 11.90 %, considering the input power of sunlight per square centimeter of the solar cell as depicted in Fig. 13d. Consequently, in the final state where the thickness of absorber layer is

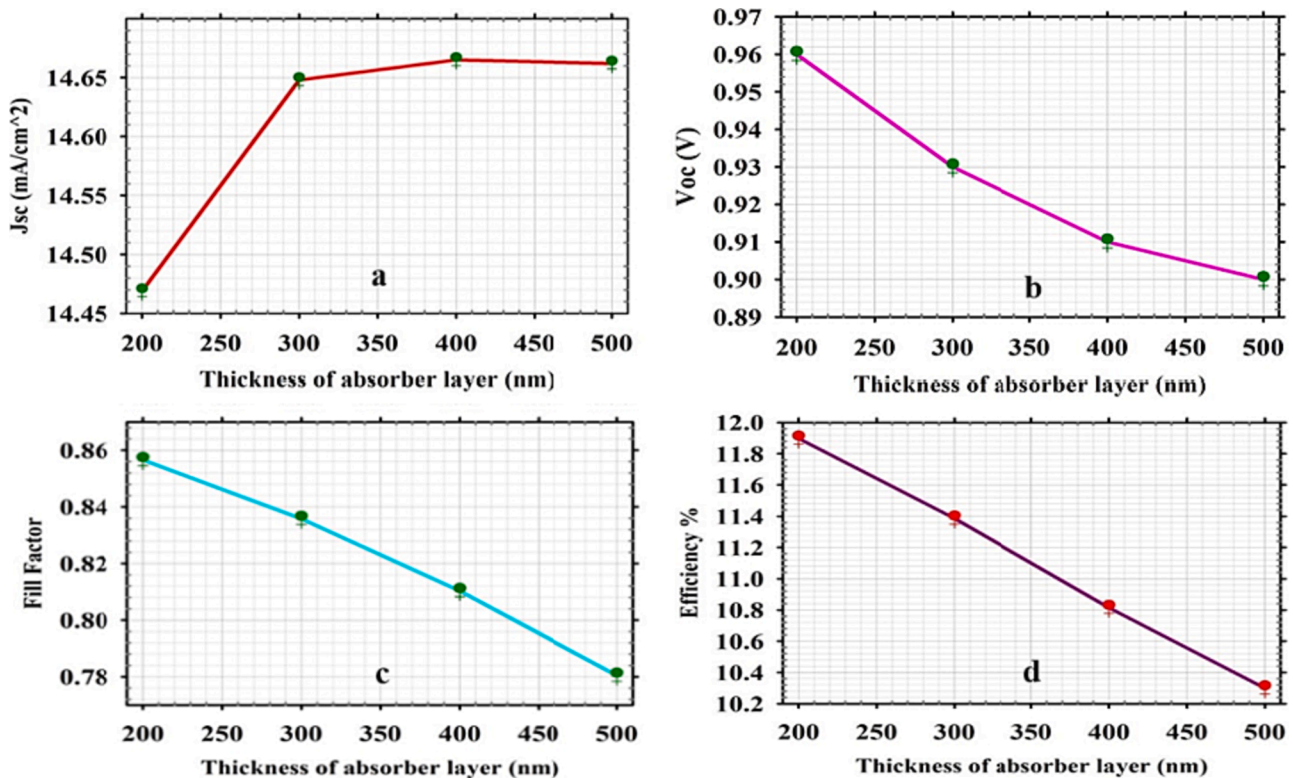


Fig. 13. Representing the variation of solar cell parameters with the thickness of absorber layer changed, where a) the short circuit current density (mA/cm<sup>2</sup>), b) the open circuit voltage (V), with different thickness of absorber layer (nm), c) the Fill Factor, and d) the final efficiency, with different thickness of absorber layer(nm).

500 nm and the ETL is 80 nm, the PCE drops to 10.29 %.

According to the results in Fig. 13, when the thickness of the absorber layer increased, two situations occurred: one, more photo-electrons were generated, so the  $J_{sc}$  was a bit increased until it was saturated. However, in the second situation, more generation rates cause more recombination. Furthermore, recombination effect happens due to the large trapped density at the interface of the ETL and perovskite layer, instigated charge trapping of electron and hole so that the  $V_{oc}$  has decreased. These two conditions impact the final PCE, as shown in Fig. 13d.

In the second scenario, where the thickness of the ETL is changed from 80 nm to 110 nm (with a light absorber layer thickness of 200 nm); Fig. 14 provides insights into the changes occurring in the components of the solar cell as the ETL thickness increases.

As shown in Fig. 14a and 14b in order, the short-circuit current exhibits a decrease within the range of  $2 \text{ mA/cm}^2$  to  $2.5 \text{ mA/cm}^2$ . Simultaneously, the open-circuit voltage gradually decreases while remaining relatively constant. The fill factor also experiences a decline, resulting in a decrease in overall efficiency (Fig. 14c). For each unit increase in thickness, the final efficiency of the solar cell drops by 2 units as illustrated in Fig. 14d. It claimed that when the thickness of the absorber layer and the ETL increase more photoelectrons experience recombination at the interface between the ETL and the light absorber layer. Based on these findings, it can be concluded that the conditions with the ETL thickness of 80 nm and the light absorber layer thickness of 200 nm result in the highest efficiency with 11.89 %.

b.  $T = 450 \text{ K}$

In this step, we are investigated the changing temperature from 300 K to 450 K on the first structure  $\text{FTO}/\text{TiO}_2/\text{RbGeBr}_3/\text{P}_3\text{HT}/\text{Au}$ , at the highest final efficiency was calculated. The obtained results indicate that the increase in short-circuit current due to temperature change from 300 K to 450 K was on the order of thousandths and did not have a significant impact on the overall current in the first structure (Fig. 15a).

However, there is a direct relationship between the open circuit

voltage and temperature, as shown by Equation (20), resulting in a decrease of 0.2 orders in the open circuit voltage (Fig. 15b). The fill factor demonstrates an inverse relationship with the cell's open circuit voltage and short circuit current, as well as a direct relationship with the cell's maximum output power, leading to a decrease of approximately 0.2 orders of magnitude (Fig. 15c). As shown in Fig. 15d, the overall PCE in this scenario, decline gradually about 1 unit in every step by increasing the temperature. Finally, it achieves 8.2% where temperature is at 450 K. Taking into account when the ETL thickness of 80 nm, the light-absorbing layer thickness of 200 nm, the HTL thickness of 300 nm, and the solar cell has got the highest PCE, a significant decline in overall productivity is observed with increasing temperature. Therefore, it can be concluded that the efficiency of the PSCs in the first structure decreases as the temperature rises.

## II. $\text{FTO}/\text{TiO}_2/\text{RbGeBr}_3/\text{P}_3\text{HT}/\text{Ag}$

a.  $T = 300 \text{ K}$

In the second structure, the layers are arranged by replacing the Au metal electrode used in the first structure with Ag. Therefore, for the second structure, the thickness of the light-absorbing layer is increased from 200 nm to 500 nm, and the thickness of the ETL is varied from 80 nm to 110 nm, while maintaining a temperature of 300 K. For the solar cells based on the first structure, four key performance factors have been identified and are presented in the following Figures. Furthermore, the J-V (current-voltage) and P-V (power-voltage) characteristics of the most efficient, where the light-absorbing layer thickness varies from 200 nm to 500 nm and the ETL thickness is 80 nm, are displayed in Fig. 16a and 16b.

The maximum short circuit current is approximately  $14.47 \text{ mA/cm}^2$  as shown in Fig. 16a, observed when the light absorber layer thickness is 200 nm and the ETL thickness remains constant at 80 nm. Fig. 16b demonstrates how the maximum power generated from the solar cell decreases as the thickness of the light-absorbing layer increases from 200 nm to 500 nm. Fig. 17 illustrates the variation of solar cell parameters with varying the thickness of the absorber layer. It shows that the

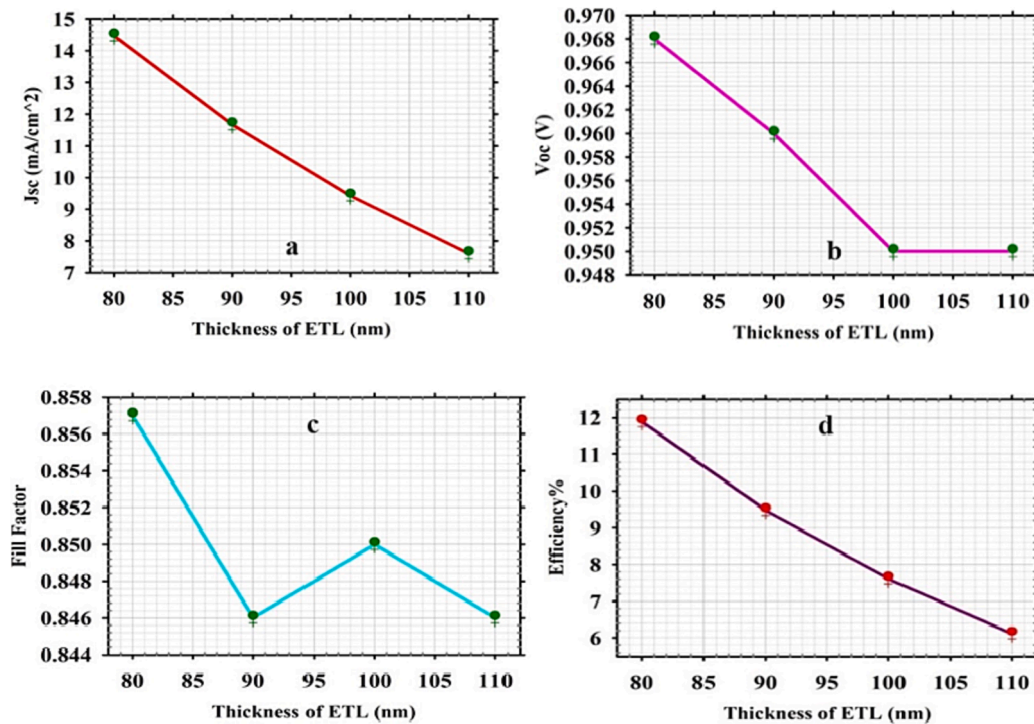


Fig. 14. Representing the variation of solar cell parameters with the thickness of ETL changed, where a) the short circuit current density ( $\text{mA/cm}^2$ ), b) the open circuit voltage (V), with different thickness of ETL (nm), c) the Fill Factor, and d) the final efficiency, with different thickness of ETL (nm).

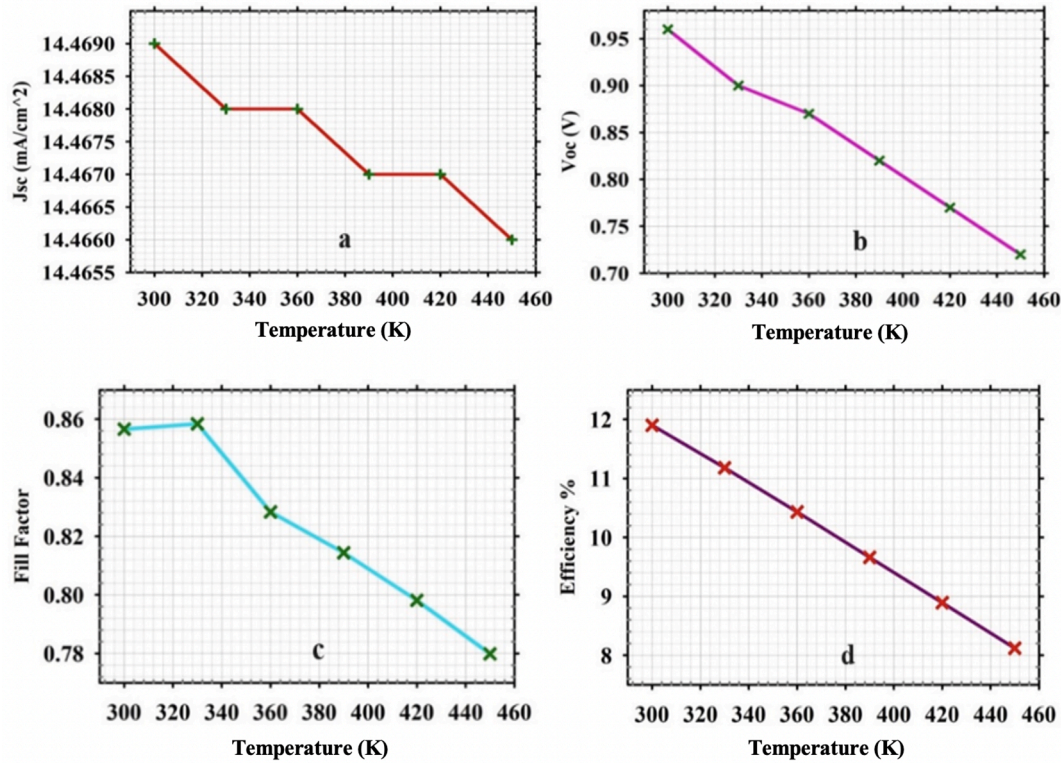


Fig. 15. Variation of solar cell parameters with the Operating temperature, where a) the short circuit current density ( $\text{mA}/\text{cm}^2$ ), b) the open circuit voltage (V), with variation of temperature from 300 K to 450 K, c) the Fill Factor, and d) the final efficiency, with variation of temperature from 300 K to 450 K.

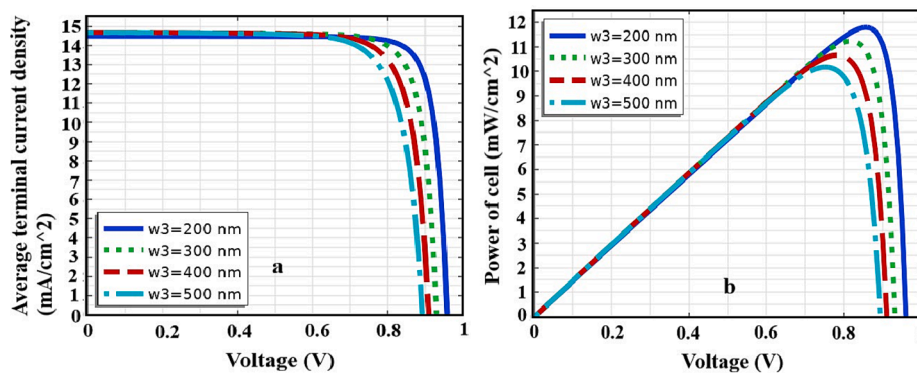


Fig. 16. a) The J-V diagram ( $\text{mA}/\text{cm}^2$ ), b) The P-V diagram ( $\text{mA}/\text{cm}^2$ ) (output power).

short circuit current increases by approximately  $0.2 \text{ mA}/\text{cm}^2$  when the light-absorbing layer thickness reaches 500 nm (Fig. 17a). The open circuit voltage experiences a decrease of around 0.1 V, and the fill factor decreases by roughly 0.1 (Fig. 17b and 17c). As depicted in Fig. 17d, in this scenario, the PCE of the PSCs decreases from its maximum value of 11.78 % to 10.173 %. This reduction is attributed to the decrease in the maximum output power of the cell and the input power from the sunlight spectrum per square centimeter. It is claimed that when the thickness of absorber layer is increased (with the thickness of the ETL keep at 80 nm), the overall PCE decreased. As the thickness of the ETL increases from 80 nm to 110 nm (with a light absorber layer thickness of 200 nm), Fig. 18 provides insights into the changes occurring in the components of the solar cell as the ETL thickness increases. In Fig. 18a, the short-circuit current shows a decrease within the range of  $2 \text{ mA}/\text{cm}^2$  to  $2.5 \text{ mA}/\text{cm}^2$  as the ETL thickness increases. Under the same conditions, the open-circuit voltage remains relatively constant between thicknesses of 80 nm to 90 nm and 100 nm to 110 nm. However, there is

a gradual decrease of approximately 0.01 V in the open-circuit voltage between thicknesses of 90 nm and 100 nm (Fig. 18b).

Furthermore, by increasing the ETL thickness from 80 nm to 90 nm, the filling factor decreases by approximately 0.005 (Fig. 18c). As shown in Fig. 18d, the PCE of the solar cell decreases by nearly 6 units, dropping from its highest value of 11.79 % at an 80 nm thickness to 6.35 % at a 110 nm thickness. As a result, by increasing the ETL thickness more photoelectrons experience recombination at the interface between the ETL and the light absorber layer. In conclusion, it can be determined that the most efficient operation, 11.78 %, of this structure is achieved when the ETL is 80 nm thick, the light-absorbing layer is 200 nm thick and the temperature at 300 K.

b.  $T = 450 \text{ K}$

In the same  $\text{FTO}/\text{TiO}_2/\text{RbGeBr}_3/\text{P}_3\text{HT}/\text{Ag}$  structure, the effect of temperature variation was investigated from 300 K to 450 K, while

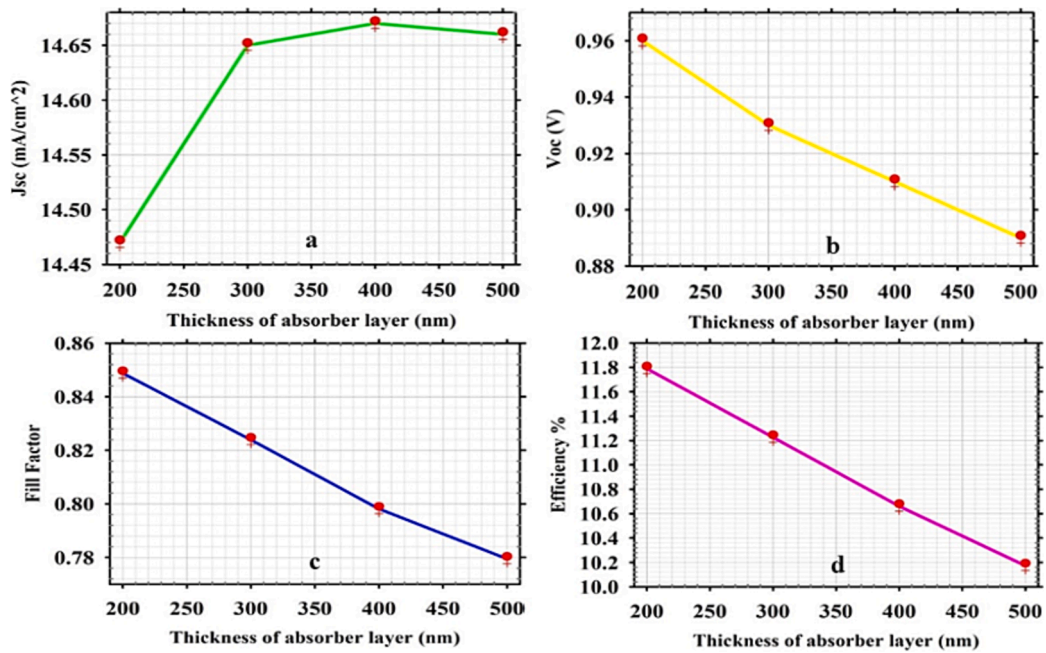


Fig. 17. Representing the variation of solar cell parameters with the thickness of absorber layer, where a) the short circuit current density (mA/cm<sup>2</sup>), b) the open circuit voltage (V), with different thickness of absorber layer (nm), c) the Fill Factor, and d) the final efficiency, with different thickness of absorber layer (nm).

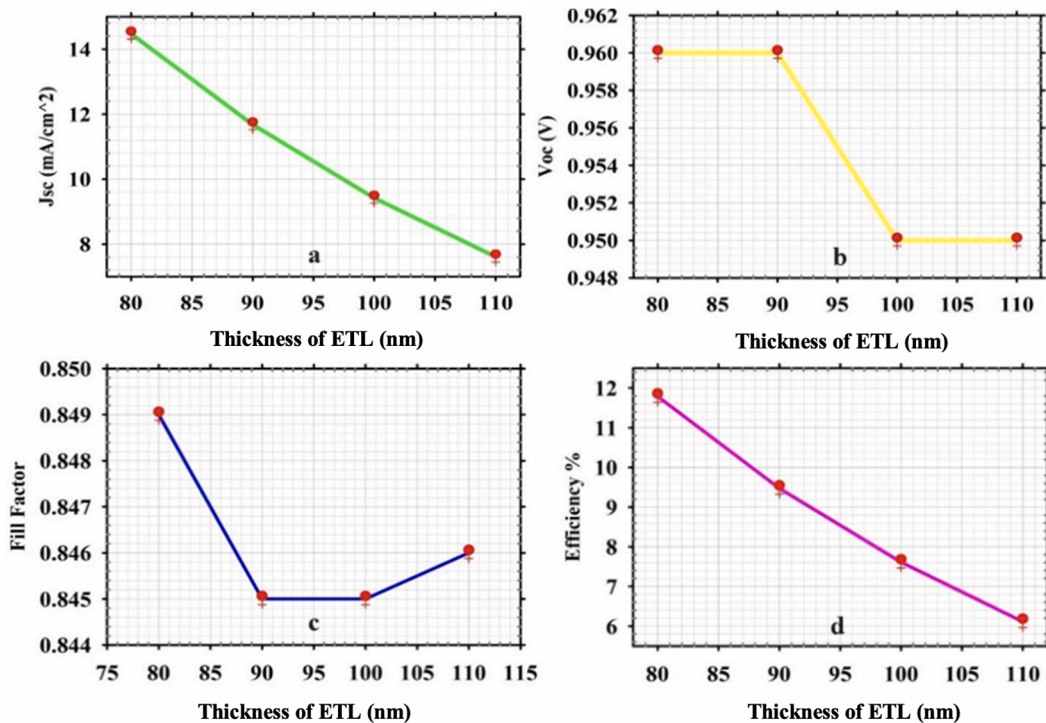


Fig. 18. The variation of solar cell parameters with the thickness of ETL, where a) the short circuit current density (ma/cm<sup>2</sup>), b) the open circuit voltage (V), with different thickness of ETL (nm), c) the Fill Factor, and d) the final efficiency, with different thickness of ETL (nm).

maintaining the structure at its highest efficiency state (with thicknesses of 80 nm for the ETL, 200 nm for the light-absorbing layer, and 300 nm for the HTL layer). Examining the J-V (current-voltage) graph, it is observed that the increase in the short circuit current due to temperature change is minimal, only a few thousandths of a current. Consequently, its impact on the overall current is negligible. However, according to Equation (20), there is a direct relationship between the open circuit

voltage and temperature. As a result, the open circuit voltage decreases by 0.2 orders, as depicted in Fig. 19a. Furthermore, the shift in open circuit voltage significantly affects the maximum output power of the cell, as illustrated in Fig. 19b. The decrease in open circuit voltage leads to a reduction in the maximum power output. Considering the data related to increasing temperatures in Fig. 20, a notable decline in overall efficiency is observed. This indicates that as the temperature rises, the

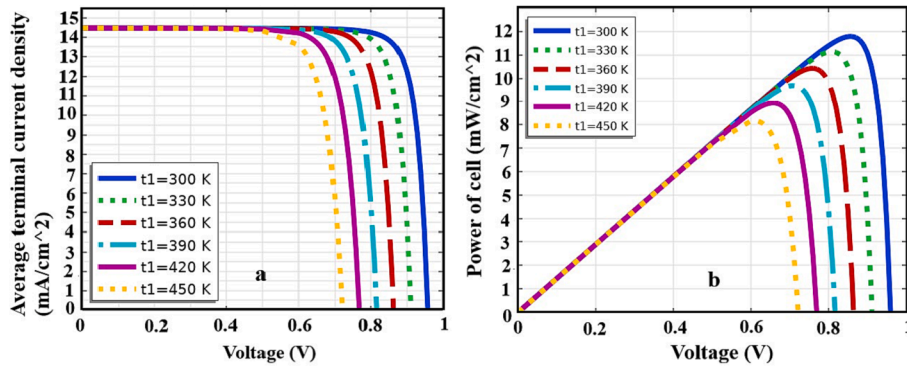


Fig. 19. a) The J-V diagram (mA/cm<sup>2</sup>), b) The P-V diagram (mA/cm<sup>2</sup>) (output power).

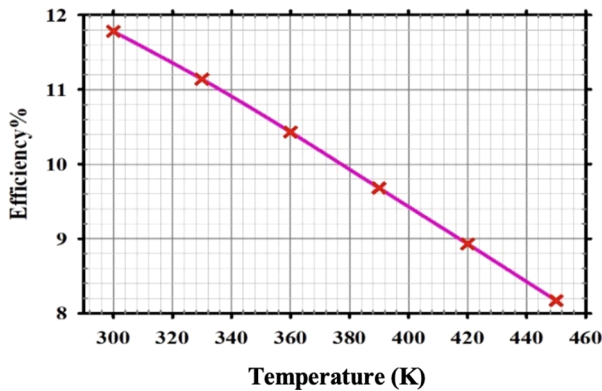


Fig. 20. Overall efficiency (%) vs temperature changes (K).

efficiency of the PSCs decreases. In conclusion, the findings highlight that increasing the temperature has an adverse effect on the overall efficiency of the PSC.

III. FTO/ITO/RbGeBr<sub>3</sub>/PEDOT:PSS/Au,  
a. T = 300 K

In the third configuration, the ETL is composed of ITO, the HTL consists of PEDOT:PSS, and the electron-collecting metal electrode is made of Au. Therefore, like the previous structures (I and II) mentioned before, the third impact is investigated in two scenarios; first, the thickness of absorber layer is increasing (with the ETL remains constant) and then in the second step, it is happened vice versa. Furthermore, in these states the temperature is stable at 300 K. In the first situation, the simulation's J-V (current-voltage) and P-V (power-voltage) graphs are

plotted at the maximum achievable efficiency with a light-absorbing layer thickness is changing from 200 nm to 500 nm, the ETL thickness of 80 nm, and the HTL thickness of 300 nm (Fig. 21a and 21b).

According to Fig. 21a, with a light absorber layer thickness of 200 nm the maximum short circuit current is approximately 14.472 mA/cm<sup>2</sup>. Fig. 21b illustrates how the maximum power generated by the solar cell decreases as the thickness of the light-absorbing layer increases from 200 nm to 500 nm. Furthermore, Fig. 22 presents the impact of the absorber layer thickness on the parameters of the solar cell. The results show that as the light-absorbing layer thickness increases while keeping the ETL thickness constant, the maximum short circuit current decreases from 14.472 mA/cm<sup>2</sup> at a thickness of 200 nm to 10.172 mA/cm<sup>2</sup> at a thickness of 500 nm (Fig. 22a). In addition, the open circuit voltage of this structure decreases from 0.96 V to 0.88 V, the fill factor decreases from 0.818 to 0.779 (Fig. 22b and 22c). Ultimately, the overall PCE of the PSCs, influenced by these three factors, decreases by 1.2 units from its maximum value of 11.374 % as depicted in Fig. 22d. Therefore, in the third structure by increasing the thickness of absorber layer (with constant ETL at 80 nm), the final operation of solar decline.

In the second step, as depicted in Fig. 23, the changes in the components of the solar cell are observed as the ETL thickness increases from 80 nm to 110 nm, with a light absorption layer thickness of 200 nm. The results indicate that the maximum short circuit current decreases from 14.472 mA/cm<sup>2</sup> to 7.606 mA/cm<sup>2</sup> as the ETL thickness increases (Fig. 23a). The open circuit voltage experiences a minor decrease of approximately 0.1 V between ETL thicknesses of 90 nm and 100 nm (Fig. 23b). Under the same conditions, the fill factor shows a slight decline of around 0.002 between 80 nm and 90 nm, but then increases by approximately 0.1 to reach a thickness of 100 nm (Fig. 23c). However, as shown in Fig. 23d, the ultimate PCE of the solar cell decreases significantly from its peak value of 11.376 % by approximately 5 units.

In conclusion, increasing the ETL thickness from 80 nm to 110 nm (with a light absorption layer thickness of 200 nm) leads to a decrease in

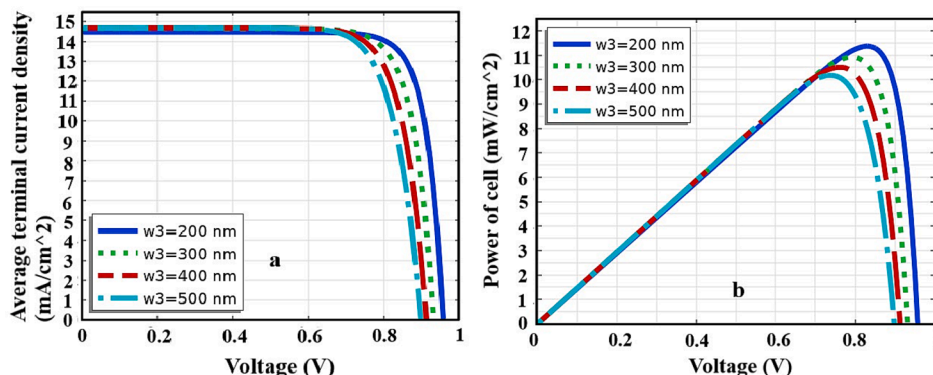


Fig. 21. a) The current-voltage (J-V), b) Power of cell (P-V) at 300 K.

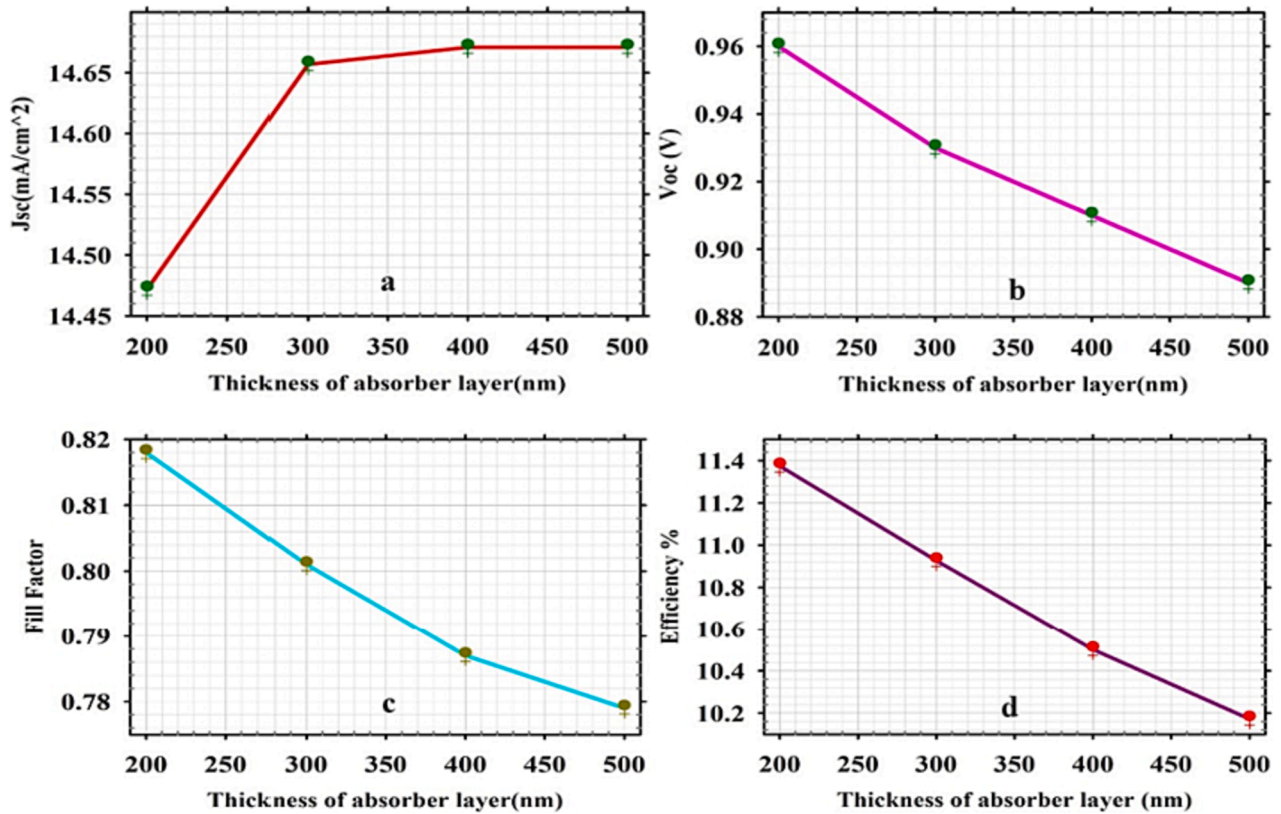


Fig. 22. The variation of solar cell parameters with the thickness of absorber layer, where a) the short circuit current density (mA/cm<sup>2</sup>), b) the open circuit voltage (V), with different thickness of absorber layer (nm), c) the Fill Factor, and d) the overall efficiency, with different thickness of absorber layer (nm).

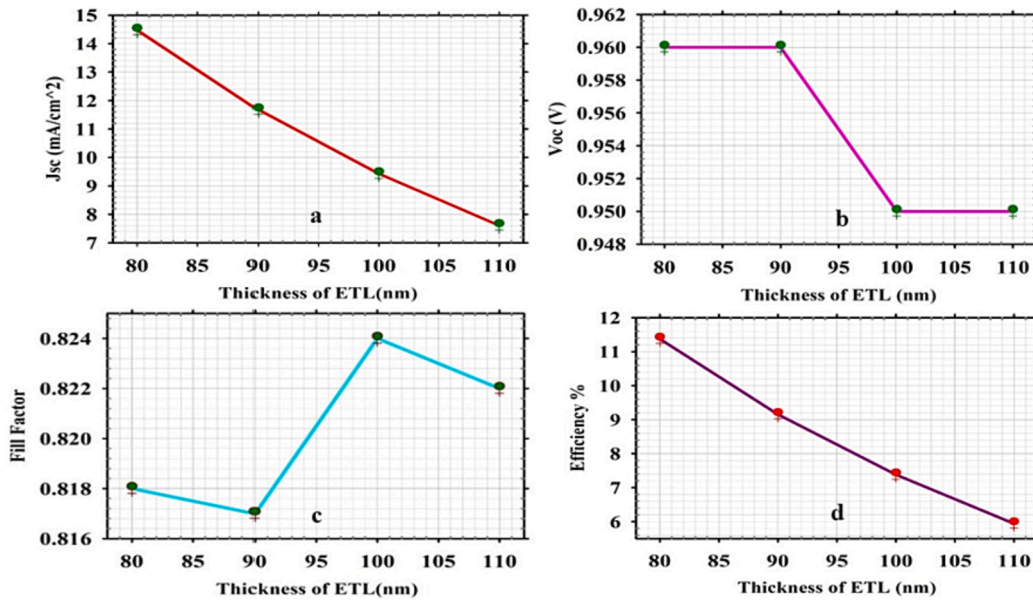


Fig. 23. The variation of solar cell parameters with the thickness of ETL, where a) the short circuit current density (mA/cm<sup>2</sup>), b) the open circuit voltage (V), with different thickness of ETL (nm), c) the Fill Factor, and d) the ultimate efficiency, with different thickness of ETL (nm).

the maximum short circuit current, a minor reduction in open circuit voltage, a variable trend in the fill factor, and a significant decline in the overall PCE of the PSCs.

b. T = 450 K

In the same structure, the effect of temperature increasing on the

third structure, FTO/ITO/RbGeBr<sub>3</sub>/PEDOT:PSS/Au, when it has obtained the highest PCE is investigated from 300 K to 450 K. The results indicate that a temperature change from 300 K to 450 K has a minimal effect on the short circuit current in the FTO/ITO/RbGeBr<sub>3</sub>/PEDOT:PSS/Au structure, with only a small increase of approximately one thousandth of the current (Fig. 24a). This change does not significantly impact the overall current in the structure. In this configuration, the

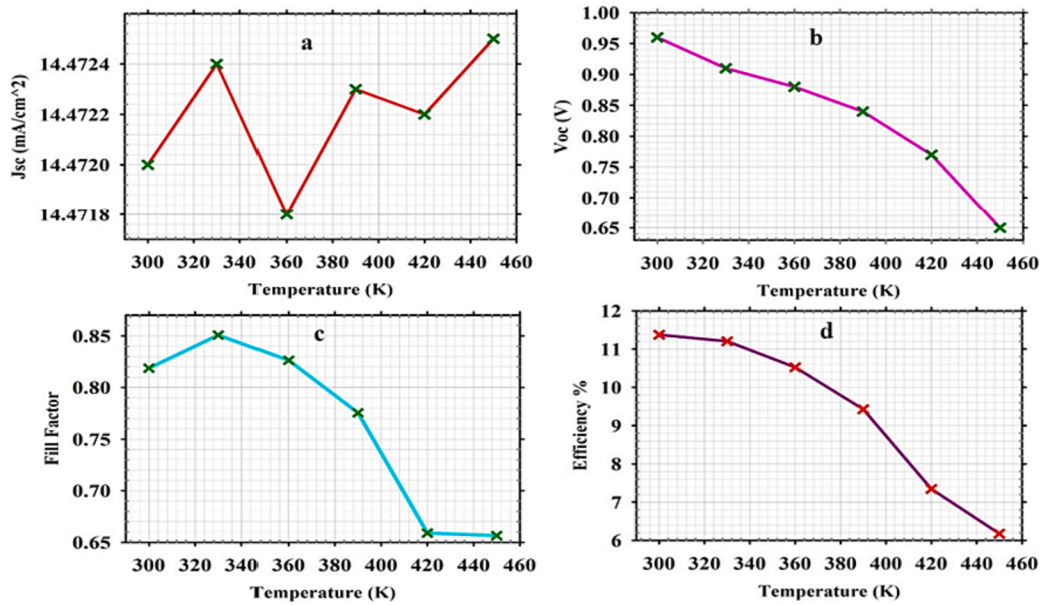


Fig. 24. Variation of solar cell parameters with the Operating temperature, where a) the short circuit current density (mA/cm<sup>2</sup>), b) the open circuit voltage (V), with variation of temperature from 300 K to 450 K, c) the Fill Factor, and d) the final efficiency (%), with variation of temperature from 300 K to 450 K.

open circuit voltage experiences a decrease of 0.3 V, which is directly related to temperature according to Equation (20) (Fig. 24b).

The fill factor demonstrates a direct relationship with the maximum output power of the cell, but an inverse relationship with the open circuit voltage and short circuit current of the cell. As a result, the fill factor shows a slight increase within the temperature range of 300 K to 330 K, followed by a decrease of approximately 0.3 orders from a temperature of 420 K, stabilizing at 0.65 (Fig. 24c). As shown in Fig. 24d, the ultimate PCE of the third impacts is influenced by increasing temperature from 300 K to 450 K, it is observed approximately 5 units decreasing. Ultimately, the highest operation of this structure is calculated when the thickness of absorber layer at 200 nm, the thickness of the ETL at 80 nm and the temperature at 300 K.

IV. FTO/ITO/RbGeBr<sub>3</sub>/PEDOT:PSS/Ag  
a. T = 300 K

In the fourth structure, the layers are sandwiched by Ag, replacing the Au metal electrode used in the third structure. At a temperature of 300 K, the thickness of the light-absorbing layer was increased from 200 nm to 500 nm, while the ETL thickness was modified from 80 nm to 110 nm. Similar to the previous structures, four key parameters for solar cells have been identified and are presented in the following Figures.

Fig. 25a and 25b illustrate the J-V (current–voltage) and P-V (power–voltage) output characteristics, respectively, for the structure with the maximum PCE. In this structure, the ETL has a thickness of 80 nm, while the thickness of the light-absorbing layer varies. In the given graphs, the thickness of the light-absorbing layer has been increased from 200 nm to 500 nm, while the thickness of the ITO remains constant at 80 nm. Considering a light-absorbing layer thickness of 200 nm.

In Fig. 25a, the solar cell exhibits a short-circuit current density of 14.473 mA/cm<sup>2</sup>, which is highly dependent on the amount of incident light radiation and its absorption by the absorber layer. The open circuit voltage is approximately 0.96 V (Fig. 25a). Additionally, when the thickness of the light-absorbing layer increases from 200 nm to 500 nm, the maximum power obtained from the product of maximum current and maximum voltage decreases from 11.27 mW/cm<sup>2</sup> to 10.17 mW/cm<sup>2</sup> (Fig. 25b). Taking into account the input power of sunlight per square centimeter, the final PCE in this scenario is calculated to be 11.372 %.

Furthermore, Fig. 26 illustrates the variation of solar cell parameters with the thickness of the absorber layer. The maximum short circuit current is approximately 14.473 mA/cm<sup>2</sup>. Increasing the light absorber layer thickness up to 500 nm results in a slight increase in the short circuit current by 0.2 mA/cm<sup>2</sup> (Fig. 26a). However, the open circuit voltage decreases from 0.96 V to approximately 0.1 V (Fig. 26b). The fill factor also decreases by approximately 0.05 (Fig. 26c). Finally, as

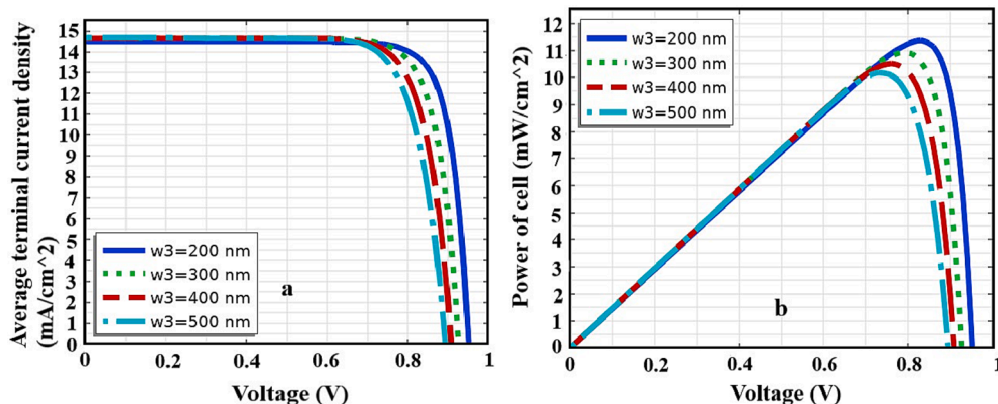


Fig. 25. a) The current–voltage (J-V), b) Power of cell (P-V) at 300 K.

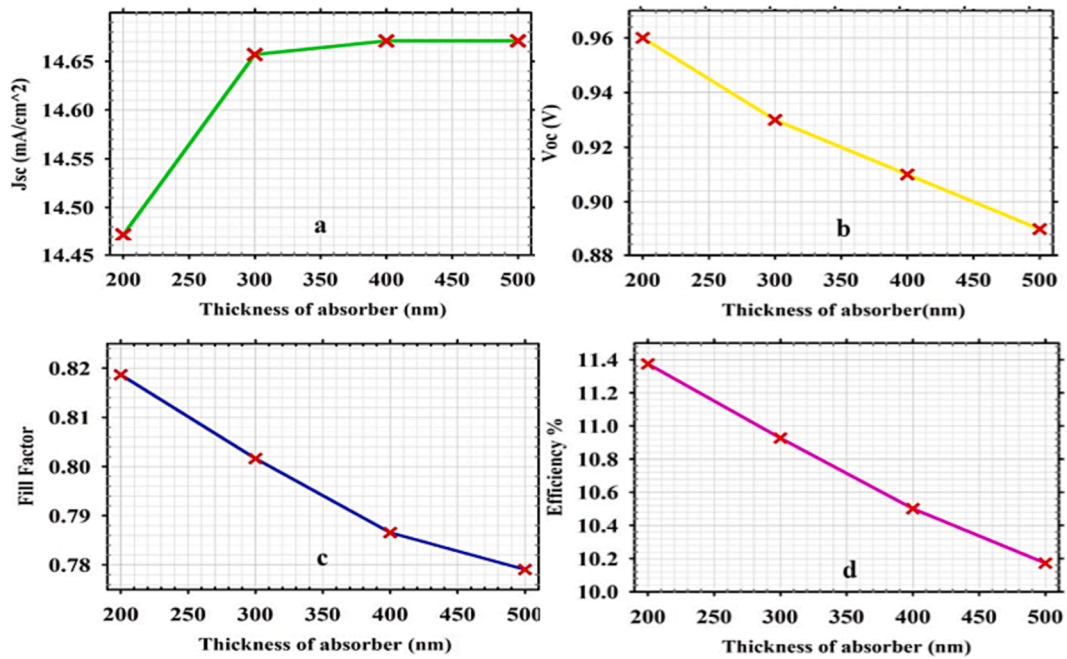


Fig. 26. The variation of solar cell parameters with the thickness of absorber layer, where a) the short circuit current density (mA/cm<sup>2</sup>), b) the open circuit voltage (V), with different thickness of absorber layer (nm), c) The Fill Factor, and d) the overall efficiency, with different thickness of absorber layer (nm).

depicted in Fig. 26d, in this case, the overall PCE decreases from its maximum value of 11.37% by 1.2 units as the light-absorbing layer thickness is extended from 200 nm to 500 nm. In the fourth structure, which involves a change in the metal contact from Au to Ag compared to the third structure, the effects were investigated by varying the thickness of both the absorber layer and ETL at a temperature of 300 K. The final results indicate that there is no significant difference between the outcomes of the third and fourth structures. As a result, the graphs for the second step (increasing the ETL thickness) were not plotted in the fourth structure.

b. T = 450 K

In the FTO/TiO<sub>2</sub>/RbGeBr<sub>3</sub>/PEDOT:PSS/Ag structure, the temperature was varied from 300 K to 450 K, while maintaining the structure with the highest PCE at a constant temperature (80 nm thickness for the ETL, 200 nm thickness for the light-absorbing layer, and 300 nm

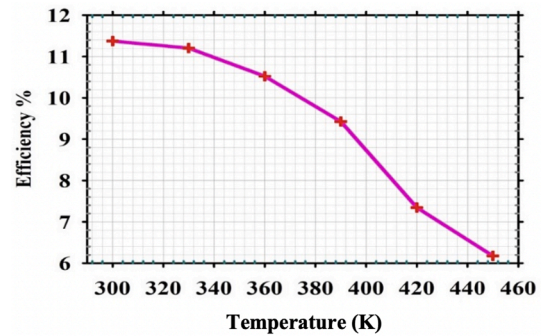


Fig. 28. Efficiency (%) vs temperature changes (K).

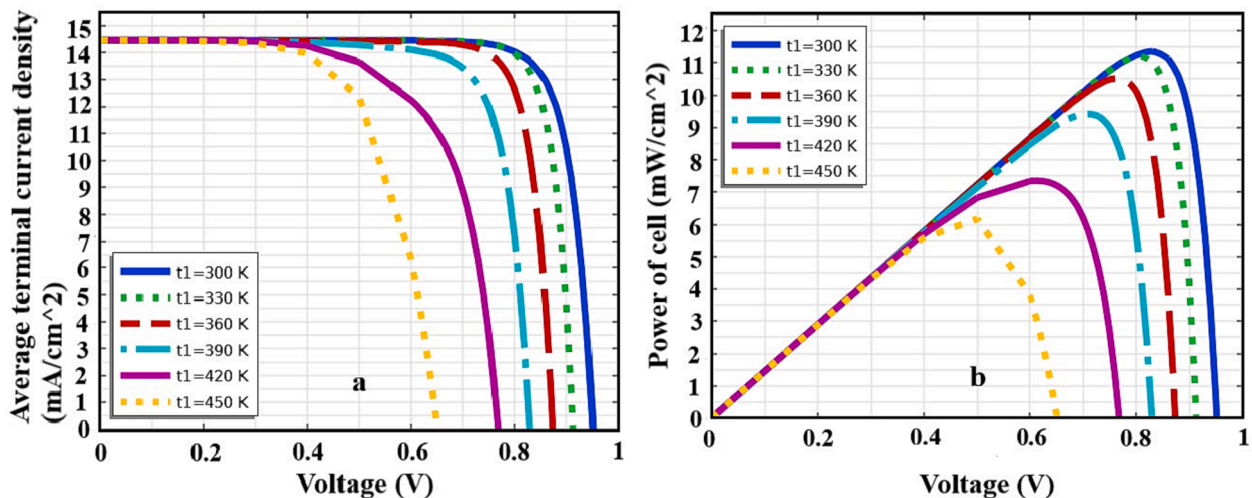



Fig. 27. a) The current–voltage (J-V), b) Power of cell (P-V) at 300 K.




**Table 2**

The highest PCE% to the lowest PCE% in the distinct structures respectively.

PCE% range	Structures	$J_{sc}$ (mA/cm <sup>2</sup> )	$V_{oc}$ (V)	FF	PCE %
The Highest 	FTO/TiO <sub>2</sub> /RbGeBr <sub>3</sub> /P <sub>3</sub> HT/Au	14.476	0.96	0.857	11.891 %
	FTO/TiO <sub>2</sub> /RbGeBr <sub>3</sub> /P <sub>3</sub> HT/Ag	14.474	0.96	0.848	11.782 %
	FTO/ITO/RbGeBr <sub>3</sub> /PEDOT : PSS/Au	14.472	0.96	0.820	11.373 %
The Lowest	FTO/ITO/RbGeBr <sub>3</sub> /PEDOT : PSS/Ag	14.471	0.96	0.817	11.370 %

**Table 3**

The effect of temperature changes on the different structures.

The effect of temperature	Structures	T = 300 K		T = 450 K		Difference of PCE%
		$V_{oc}$ (V)	PCE%	$V_{oc}$ (V)	PCE%	
More Stable 	FTO/TiO <sub>2</sub> /RbGeBr <sub>3</sub> /P <sub>3</sub> HT/Ag	0.96	11.78	0.73	8.17	3.61
	FTO/TiO <sub>2</sub> /RbGeBr <sub>3</sub> /P <sub>3</sub> HT/Au	0.96	11.89	0.73	8.12	3.77
	FTO/ITO/RbGeBr <sub>3</sub> /PEDOT : PSS/Au	0.96	11.37	0.65	6.18	5.19
Unstable	FTO/ITO/RbGeBr <sub>3</sub> /PEDOT : PSS/Ag	0.96	11.37	0.66	6.17	5.20

thickness for the HTL). The investigation was conducted similarly to the previous structures. Based on the J-V and P-V graphs, it can be observed that the increase in the short circuit current due to the temperature change is minimal, only on the order of thousandths, indicating a negligible impact on the overall current (Fig. 27a). Equation (20), which states the direct correlation between open-circuit voltage and temperature, is consistent with the results. The open circuit voltage decreases by 0.3 orders as the temperature is increased (Fig. 27b). Considering the output results obtained from varying the temperature, a significant decrease in the ultimate efficiency of the PSCs is observed, with a decline of approximately five units (Fig. 28). In conclusion, raising the temperature has an adverse effect on the overall PCE of the PSCs, as indicated by the decrease in efficiency with increasing temperature.

Comparing the fourth structure with the third structure, which differs only in the metal electrode layer, the results and Figures indicate that there is no significant change in the overall efficiency. Whether gold or silver is used as the metal electrode, the ultimate efficiency remains relatively consistent. Both Au and Ag are viable options for serving as the electron-collecting metal electrode in PSCs. Au is commonly studied due to its relatively high work function ( $\varphi_m = 5.10\text{eV}$ ) and is often compared to Ag, which possesses a lower work function ( $\varphi_m = 4.26\text{eV}$ ). The general observation is that the shunt resistance and open-circuit voltage of the devices tend to decrease with the diminishing work function of the contact metal, resulting in a sloped current density curve (J-V) at the short circuit point [76]. Furthermore, in the case of low work function metals such as Ag, there is an electron transfer from the Fermi level of the metal into the conduction band of the perovskite and decrease the open-circuit voltage. Ag devices exhibit characteristics similar to other low work function metals, like Chromium and Copper, and tend to have the lowest values due to the easy recombination of photoelectrons at the metal interface. However, the primary consideration for using Ag as the back contact is its cost-effectiveness compared to Au. The results are summarized in Table 2.

These results reinforce the notion that the efficiency of PSCs is significantly influenced by various factors. The choice of semiconductor material used for different layers, the optimal thickness of these layers, and the environmental temperature are some of the key factors that play a more prominent role in determining the overall efficiency of the solar cell (Table 3).

In this study, four different structures are discussed in Section “Discussions and Results”, each featuring all-mineral PSCs with an inorganic perovskite, RbGeBr<sub>3</sub>, as the absorber active layer—a novel addition to

the field. Crucial parameters for all the solar cells are meticulously calculated and compared. While recent years have seen extensive theoretical and experimental research on cesium in various compositions like CsPbX<sub>3</sub>, CsSnX<sub>3</sub> (as proposed in Section “Structure design method of PSCs with RbGeBr<sub>3</sub> inorganic active layer”), and CsGeI<sub>3</sub>, numerical calculations have also been explored for other elements of the first group using Density Function Theory (DFT), such as RbGeX<sub>3</sub> and KGeX<sub>3</sub> [56,57]. For instance, experimental research on inorganic PSCs based on CsSnBr<sub>3</sub> has shown notable performance with a short-circuit current ( $J_{sc}$ ) of 21.23 mA/cm<sup>2</sup>, an open-circuit voltage ( $V_{oc}$ ) of 0.85 V, and a PCE of 10.46 % using the ITO/TiO<sub>2</sub>/CsSnBr<sub>3</sub>/Spiro-OMeTAD/Au structure [36,49]. A theoretical investigation on a mineral PSCs based on CsSnI<sub>3</sub>, including the ITO/TiO<sub>2</sub>/CsSnI<sub>3</sub>/Spiro-OMeTAD/Au structure, revealed a short-circuit current of 16.80 mA/cm<sup>2</sup>, an open-circuit voltage of 0.88 V, and a PCE of 6.40 % under AM1.5 G [48]. In comparison, this current study demonstrates superior performance with the highest short-circuit current of 14.47 mA/cm<sup>2</sup>, an open-circuit voltage of 0.96 V, and the highest PCE of 11.98 %. This validation underscores the potential of RbGeBr<sub>3</sub> as a subject for further exploration as a light-absorbing layer in inorganic PSCs.

## Conclusion

In this research, we conducted an investigation into the potential of RbGeBr<sub>3</sub> as a light-absorbing mineral active layer for four distinct PSCs. Additionally, in all structures with thicknesses of 80 nm for the ETL, 200 nm for the light-absorbing mineral layer, and 300 nm (constant value) for the HTL obtained the highest PCE. Among the studied configurations, the first structure, FTO/TiO<sub>2</sub>/RbGeBr<sub>3</sub>/P<sub>3</sub>HT/Au, achieved the highest PCE, reaching 11.891 %, with a short-circuit current of 14.476 mA/cm<sup>2</sup> and an open-circuit voltage of 0.96 V. Furthermore, the PCE of the other structures are 11.782 %, 11.373 % and 11.37 % refer to the second, third and fourth structures, respectively. All the items have exhibited an open-circuit voltage of 0.96 V and a slight difference in a short-circuit current. The study also investigated the conditions yielding the highest efficiency for all four structures at temperatures ranging from 300 K to 450 K. The overall results indicate that the second structure, FTO/TiO<sub>2</sub>/RbGeBr<sub>3</sub>/P<sub>3</sub>HT/Ag, is more stable at temperature. The PCE at 300 K is 11.78 % reaching 8.17 % at 450 K, which shows a 3.61 unit difference. Additionally, the final results illustrate that the stability of the structures decrease from the first structure (3.77 of unit difference), the third structure (5.19 of unit difference) and the fourth

structure (5.20 of difference) respectively. This research report could serve as a valuable guide for future investigations of this material in more intricate cells to enhance PCE.

### Feasibility of the work

The primary objective of this study was to scrutinize the potential of utilizing inorganic perovskite material as a light-absorbing layer and understanding its performance within a PSCs. Given the current high costs associated with manufacturing solar cells, a pragmatic and logical approach involves an initial assessment of solar cells through diverse simulation methods. This strategic step allows for the evaluation of different scenarios, and if satisfactory outcomes are achieved, the subsequent phase involves the experimental validation of the envisioned solar cell [34,36,49]. Due to the lack of prior theoretical or experimental exploration of this material, a theoretical investigation was conducted using the COMSOL Multiphysics simulator. The outcomes of this research revealed the material's potential suitability for use as a light-absorbing layer in solar cells.

Alternatively, various fabrication methods such as spin coating method, synthesis method and ultrasonic spray can be employed to enhance the overall efficiency of cells [77–79]. This approach aims to make the efficiency of the structures tested in this study more acceptable. For instance, optimizing hole and electron transporting materials and combining them with other substances can be explored to improve their stability under diverse environmental conditions [26,27,80–82].

It is considered both reasonable and logical to enhance the efficiency of these structures for industrial production by incorporating other light-absorbing layers that have been experimentally studied and have yielded satisfactory results [17,18,32,34,83]. This strategic approach contributes to an overall improvement in the efficiency of the structures.

Additionally, it is crucial to consider that the fabrication method of these cells, the environmental conditions during manufacturing, the precision and methodology of layering these materials atop one another, and even the morphology of the material itself significantly influence the final efficiency achieved in experimental studies and testing [84–87]. These factors collectively play a pivotal role in determining the overall performance of the solar cells.

### CRedit authorship contribution statement

**Shima Valizadeh:** Writing – review & editing, Writing – original draft, Visualization, Validation, Software, Methodology, Investigation, Formal analysis, Data curation, Conceptualization. **Aliasghar Shokri:** Conceptualization, Data curation, Formal analysis, Methodology, Project administration, Supervision, Validation, Visualization, Writing – review & editing. **Amirabbas Sabouri-Dodaran:** Visualization, Validation, Supervision, Methodology, Investigation, Data curation, Conceptualization. **Nazila Fough:** Writing – review & editing, Visualization, Validation, Investigation. **Firdaus Muhammad-Sukki:** Writing – review & editing, Visualization, Validation, Investigation.

### Declaration of competing interest

The authors declare that they have no known competing financial interests or personal relationships that could have appeared to influence the work reported in this paper.

### Data availability

Data will be made available on request.

### Acknowledgement

Firdaus Muhammad-Sukki would like to acknowledge the funding from Royal Society of Edinburgh (RSE) Personal Research Fellowship

Award (Project ID: 3204).

### References

- [1] Sum TC, Mathews N. Advancements in perovskite solar cells: Photophysics behind the photovoltaics. *Energy Environ Sci* 2014;7:2518–34. <https://doi.org/10.1039/C4EE00673A>.
- [2] Elangovan NK, Arumugam S, Chayaver. Indian-traditional dye to modern dye-sensitized solar cells. *Mater Res Express* 2019;6:066206. <https://doi.org/10.1088/2053-1591/AB0CAD>.
- [3] Ho Lee J, Su Jin I, Woong Jung J. Binary-mixed organic electron transport layers for planar heterojunction perovskite solar cells with high efficiency and thermal reliability. *Chem Eng J* 2021;420:129678. <https://doi.org/10.1016/J.CEJ.2021.129678>.
- [4] Chung J, Shin SS, Hwang K, Kim G, Kim KW, Lee DS, et al. Record-efficiency flexible perovskite solar cell and module enabled by a porous-planar structure as an electron transport layer. *Energy Environ Sci* 2020;13:4854–61. <https://doi.org/10.1039/D0EE02164D>.
- [5] Chen S, Xiao X, Gu H, Huang J. Iodine reduction for reproducible and high-performance perovskite solar cells and modules. *Sci Adv* 2021;7. [https://doi.org/10.1126/SCIADV.ABE8130/SUPPL\\_FILE/ABE8130\\_SM.PDF](https://doi.org/10.1126/SCIADV.ABE8130/SUPPL_FILE/ABE8130_SM.PDF).
- [6] Li Z, Gao Y, Zhang Z, Xiong Q, Deng L, Li X, et al. cPCN-Regulated SnO<sub>2</sub> Composites Enables Perovskite Solar Cell with Efficiency Beyond 23%. *Nanomicro Lett* 2021;13:1–16. <https://doi.org/10.1007/s40820-021-00636-0/FIGURES/6>.
- [7] Wang H, Dong Z, Liu H, Li W, Zhu L, Chen H. Roles of Organic Molecules in Inorganic CsPbX<sub>3</sub> Perovskite Solar Cells. *Adv Energy Mater* 2021;11:2002940. <https://doi.org/10.1002/AENM.202002940>.
- [8] De Wolf S, Holovsky J, Moon SJ, Löper P, Niesen B, Ledinsky M, et al. Organometallic halide perovskites: Sharp optical absorption edge and its relation to photovoltaic performance. *J Phys Chem Lett* 2014;5:1035–9. [https://doi.org/10.1021/JZ500279B/SUPPL\\_FILE/JZ500279B\\_SI\\_001.PDF](https://doi.org/10.1021/JZ500279B/SUPPL_FILE/JZ500279B_SI_001.PDF).
- [9] D'Innocenzo V, Grancini G, Alcocer MJP, Kandada ARS, Stranks SD, Lee MM, et al. Excitons versus free charges in organo-lead tri-halide perovskites. *Nat Commun* 2014;5:1–6. <https://doi.org/10.1038/ncomms4586>.
- [10] Manser JS, Kamat PV. Band filling with free charge carriers in organometallic halide perovskites. *Nat Photonics* 2014;8:737–43. <https://doi.org/10.1038/nphoton.2014.171>.
- [11] Stranks SD, Eperon GE, Grancini G, Menelaou C, Alcocer MJP, Leijtens T, et al. Electron-hole diffusion lengths exceeding 1 micrometer in an organometallic trihalide perovskite absorber. *Science* 2013;342:341–4. [https://doi.org/10.1126/SCIENC.E.1243982/SUPPL\\_FILE/STRANKS-SM.PDF](https://doi.org/10.1126/SCIENC.E.1243982/SUPPL_FILE/STRANKS-SM.PDF).
- [12] Aharon S, Dymshits A, Rotem A, Etgar L. Temperature dependence of hole conductor free formamidinium lead iodide perovskite based solar cells. *J Mater Chem A Mater* 2015;3:9171–8. <https://doi.org/10.1039/C4TA05149A>.
- [13] Sahare S, Pham HD, Angmo D, Ghoderao P, MacLeod J, Khan SB, et al. Emerging Perovskite Solar Cell Technology: Remedial Actions for the Foremost Challenges. *Adv Energy Mater* 2021;11:2101085. <https://doi.org/10.1002/AENM.202101085>.
- [14] Green MA, Ho-Baillie A, Snaith HJ. The emergence of perovskite solar cells. *Nat Photonics* 2014;8:506–14. <https://doi.org/10.1038/nphoton.2014.134>.
- [15] Egger DA, Kronik L. Role of dispersive interactions in determining structural properties of organic-inorganic halide perovskites: Insights from first-principles calculations. *J Phys Chem Lett* 2014;5:2728–33. [https://doi.org/10.1021/JZ5012934/ASSET/IMAGES/MEDIUM/JZ-2014-012934\\_0005.GIF](https://doi.org/10.1021/JZ5012934/ASSET/IMAGES/MEDIUM/JZ-2014-012934_0005.GIF).
- [16] Chen Q, De Marco N, Yang Y, Song T Bin, Chen CC, Zhao H, et al. Under the spotlight: The organic-inorganic hybrid halide perovskite for optoelectronic applications. *Nano Today* 2015;10:355–96. <https://doi.org/10.1016/J.NANTOD.2015.04.009>.
- [17] Mohammadi MH, Fathi D, Eskandari M. Light trapping in perovskite solar cells with plasmonic core/shell nanorod array: A numerical study. *Energy Rep* 2021;7:1404–15. <https://doi.org/10.1016/J.EGYR.2021.02.071>.
- [18] Majidi M, Eskandari M, Fathi D. Textured HTM-free perovskite/PbS quantum dot solar cell: Optical and electrical efficiency improvement by light trapping control. *Solar Energy* 2021;230:618–27. <https://doi.org/10.1016/J.SOLENER.2021.10.008>.
- [19] Aliyariyan M, Fathi D, Eskandari M, Mohammadi MH. Simulation and investigation of perovskite/nano-pyramidal GeSe solar cell: Realizing high efficiency by controllable light trapping. *Solar Energy* 2021;214:310–8. <https://doi.org/10.1016/J.SOLENER.2020.11.063>.
- [20] Mohammadi MH, Eskandari M, Fathi D. Effects of the location and size of plasmonic nanoparticles (Ag and Au) in improving the optical absorption and efficiency of perovskite solar cells. *J Alloys Compd* 2021;877:160177. <https://doi.org/10.1016/J.JALLCOM.2021.160177>.
- [21] Mohammadi MH, Eskandari M, Fathi D. Improving the efficiency of perovskite solar cells via embedding random plasmonic nanoparticles: Optical-electrical study on device architectures. *Solar Energy* 2021;221:162–75. <https://doi.org/10.1016/J.SOLENER.2021.04.038>.
- [22] Solhtalab N, Mohammadi MH, Eskandari M, Fathi D. Efficiency improvement of half-tandem CIGS/perovskite solar cell by designing nano-prism nanostructure as the controllable light trapping. *Energy Reports* 2022;8:1298–308. <https://doi.org/10.1016/J.EGYR.2021.12.038>.
- [23] Fooladvand P, Eskandari M, Fathi D, Das N. Single-walled carbon nanotube as hole transport layer in perovskite solar cell: Efficiency enhancement. *Energy Reports* 2023;10:3652–64. <https://doi.org/10.1016/J.EGYR.2023.10.020>.
- [24] Mohammadi MH, Eskandari M, Fathi D. Design of optimized photonic-structure and analysis of adding a SiO<sub>2</sub> layer on the parallel CH<sub>3</sub>NH<sub>3</sub>PbI<sub>3</sub>/CH<sub>3</sub>NH<sub>3</sub>SnI<sub>3</sub>

- perovskite solar cells. *Scientific Reports* 2023;13:1–19. <https://doi.org/10.1038/s41598-023-43137-3>.
- [25] Liang H, Wen Z, Wang F, Cheng Z. Design of hierarchical nanohole for efficient broadband light absorption of MAPbI<sub>3</sub> perovskite material based solar cell with thin absorber layer. *Energy Reports* 2023;9:190–8. <https://doi.org/10.1016/j.egyrep.2023.03.001>.
- [26] Mohammadi MH, Fathi D, Eskandari M. NiO@GeSe core-shell nano-rod array as a new hole transfer layer in perovskite solar cells: A numerical study. *Solar Energy* 2020;204:200–7. <https://doi.org/10.1016/j.solener.2020.04.038>.
- [27] Maleki J, Eskandari M, Fathi D. PbSe<sub>2</sub>-grating as new hole transport layer in perovskite solar cells: Superior efficiency enhancement thru simulation and optimization. *J Alloys Compd* 2023;960:170653. <https://doi.org/10.1016/j.jallcom.2023.170653>.
- [28] Tooghi A, Fathi D, Eskandari M. High-performance perovskite solar cell using photonic-plasmonic nanostructure. *Scientific Reports* 2020;10:1–13. <https://doi.org/10.1038/s41598-020-67741-9>.
- [29] Mohammadi MH, Eskandari M, Fathi D. Morphological investigation and 3D simulation of plasmonic nanostructures to improve the efficiency of perovskite solar cells. *Scientific Reports* 2023;13:1–12. <https://doi.org/10.1038/s41598-023-46098-9>.
- [30] Seo J, Noh JH, Seok SII. Rational Strategies for Efficient Perovskite Solar Cells. *Acc Chem Res* 2016;49:562–72. <https://doi.org/10.1021/acs.accounts.5b00444>. <https://doi.org/10.1021/ACSACCOUNTS.5B00444.ASSET/IMAGES/MEDIUM/AR-2015-00444P.0013.GIF>.
- [31] Stranks SD, Snaith HJ. Metal-halide perovskites for photovoltaic and light-emitting devices. *Nature Nanotechnology* 2015;10:391–402. <https://doi.org/10.1038/nnano.2015.90>.
- [32] Zhang YY, Chen S, Xu P, Xiang H, Gong XG, Walsh A, et al. Intrinsic Instability of the Hybrid Halide Perovskite Semiconductor CH<sub>3</sub>NH<sub>3</sub>PbI<sub>3</sub>\*. *Chinese Physics Letters* 2018;35:036104. <https://doi.org/10.1088/0256-307X/35/3/036104>.
- [33] Luo YX, Xie FM, Chen JDe, Ren H, Wang JK, Cai XY, et al. Uniform Stepped Interfacial Energy Level Structure Boosts Efficiency and Stability of CsPbI<sub>2</sub>Br Solar Cells. *Adv Funct Mater* 2021;31:2103316. <https://doi.org/10.1002/ADFM.202103316>.
- [34] Kulbak M, Gupta S, Kedem N, Levine I, Bendikov T, Hodes G, et al. Cesium Enhances Long-Term Stability of Lead Bromide Perovskite-Based Solar Cells. *J Phys Chem Lett* 2016;7:167–72. <https://doi.org/10.1021/acs.jpcclett.5b02597>. [https://doi.org/10.1021/ACSJPCCLETT.5B02597.SUPPL\\_FILE/JZ5B02597\\_SI\\_001.PDF](https://doi.org/10.1021/ACSJPCCLETT.5B02597.SUPPL_FILE/JZ5B02597_SI_001.PDF).
- [35] Hossain MK, Toki GFI, Madan J, Pandey R, Bencherif H, Mohammed MKA, et al. A comprehensive study of the optimization and comparison of cesium halide perovskite solar cells using ZnO and Cu<sub>2</sub>FeSn<sub>4</sub> as charge transport layers. *New Journal of Chemistry* 2023;47:8602–24. <https://doi.org/10.1039/D3NJ00320E>.
- [36] Chen LJ, Lee CR, Chuang YJ, Wu ZH, Chen C. Synthesis and Optical Properties of Lead-Free Cesium Tin Halide Perovskite Quantum Rods with High-Performance Solar Cell Application. *J Phys Chem Lett* 2016;7:5028–35. <https://doi.org/10.1021/acs.jpcclett.6b02344>. [https://doi.org/10.1021/ACSJPCCLETT.6B02344.SUPPL\\_FILE/JZ6B02344\\_SI\\_001.PDF](https://doi.org/10.1021/ACSJPCCLETT.6B02344.SUPPL_FILE/JZ6B02344_SI_001.PDF).
- [37] Ye T, Wang X, Wang K, Ma S, Yang D, Hou Y, et al. Localized Electron Density Engineering for Stabilized B<sup>2+</sup>CsSnI<sub>3</sub>-Based Perovskite Solar Cells with Efficiencies >10%. *ACS Energy Lett* 2021;6:1480–9. <https://doi.org/10.1021/acsenenergylett.1c00342>. [https://doi.org/10.1021/ACSENERGYLETT.1C00342.SUPPL\\_FILE/NZ1C00342\\_SI\\_001.PDF](https://doi.org/10.1021/ACSENERGYLETT.1C00342.SUPPL_FILE/NZ1C00342_SI_001.PDF).
- [38] Hossain MK, Rubel MHK, Toki GFI, Alam I, Rahman MF, Bencherif H. Effect of Various Electron and Hole Transport Layers on the Performance of CsPbI<sub>3</sub>-Based Perovskite Solar Cells: A Numerical Investigation in DFT, SCAPS-1D, and wxAMPS Frameworks. *ACS Omega* 2022;7:43210–30. <https://doi.org/10.1021/acsomega.2c005912>. <https://doi.org/10.1021/ACSOMEGA.2C005912/ASSET/IMAGES/LARGE/AO2C005912.0013.JPEG>.
- [39] Wang R, Mujahid M, Duan Y, Wang ZK, Xue J, Yang Y. A Review of Perovskites Solar Cell Stability. *Adv Funct Mater* 2019;29:1808843. <https://doi.org/10.1002/ADFM.201808843>.
- [40] Akbulatov AF, Luchkin SY, Frolova LA, Dremova NN, Gerasimov KL, Zhidkov IS, et al. Probing the Intrinsic Thermal and Photochemical Stability of Hybrid and Inorganic Lead Halide Perovskites. *J Phys Chem Lett* 2017;8:1211–8. <https://doi.org/10.1021/acs.jpcclett.6b03026>. [https://doi.org/10.1021/ACSJPCCLETT.6B03026.SUPPL\\_FILE/JZ6B03026\\_SI\\_001.PDF](https://doi.org/10.1021/ACSJPCCLETT.6B03026.SUPPL_FILE/JZ6B03026_SI_001.PDF).
- [41] Eperon GE, Paternò GM, Sutton RJ, Zampetti A, Haghighirad AA, Cacialli F, et al. Inorganic caesium lead iodide perovskite solar cells. *J Mater Chem A Mater* 2015;3:19688–95. <https://doi.org/10.1039/C5TA06398A>.
- [42] Zeng Q, Zhang X, Liu C, Feng T, Chen Z, Zhang W, et al. Inorganic CsPbI<sub>2</sub>Br Perovskite Solar Cells: The Progress and Perspective. *Solar RRL* 2019;3:1800239. <https://doi.org/10.1002/SOLR.201800239>.
- [43] Tooghi A, Fathi D, Eskandari M. Numerical study of a highly efficient light trapping nanostructure of perovskite solar cell on a textured silicon substrate. *Scientific Reports* 2020;10:1–13. <https://doi.org/10.1038/s41598-020-75630-4>.
- [44] Rubel MHK, Hossain MA, Hossain MK, Hossain KM, Khatun AA, Rahaman MM, et al. First-principles calculations to investigate structural, elastic, electronic, thermodynamic, and thermoelectric properties of CaPd<sub>3</sub>B<sub>4</sub>O<sub>12</sub> (B = Ti, V) perovskites. *Results Phys* 2022;42:105977. <https://doi.org/10.1016/j.rinp.2022.105977>.
- [45] Hossain MK, Arnab AA, Das RC, Hossain KM, Rubel MHK, Rahman MF, et al. Combined DFT, SCAPS-1D, and wxAMPS frameworks for design optimization of efficient Cs<sub>2</sub>BiAgI<sub>6</sub>-based perovskite solar cells with different charge transport layers. *RSC Adv* 2022;12:35002–25. <https://doi.org/10.1039/D2RA06734J>.
- [46] Bouhmaidit S, Uddin MB, Pingak RK, Ahmad S, Rubel MHK, Hakamy A, et al. Investigation of heavy thallium perovskites TlGeX<sub>3</sub> (X = Cl, Br and I) for optoelectronic and thermoelectric applications: A DFT study. *Mater Today Commun* 2023;37:107025. <https://doi.org/10.1016/j.mtcomm.2023.107025>.
- [47] Rahaman MM, Hossain KM, Rubel MHK, Islam AKMA, Kojima S. Alkaline-Earth Metal Effects on Physical Properties of Ferromagnetic AVO<sub>3</sub> (A = Ba, Sr, Ca, and Mg): Density Functional Theory Insights. *ACS Omega* 2022;7:20914–26. <https://doi.org/10.1021/ACSOMEGA.2C01630>. [https://doi.org/10.1021/ACSOMEGA.2C01630/ASSET/IMAGES/MEDIUM/AO2C01630\\_M011.GIF](https://doi.org/10.1021/ACSOMEGA.2C01630/ASSET/IMAGES/MEDIUM/AO2C01630_M011.GIF).
- [48] Hossain MK, Toki GFI, Samajdar DP, Mushtaq M, Rubel MHK, Pandey R, et al. Deep Insights into the Coupled Optoelectronic and Photovoltaic Analysis of Lead-Free CsSnI<sub>3</sub> Perovskite-Based Solar Cell Using DFT Calculations and SCAPS-1D Simulations. *ACS Omega* 2023;8:22466–85. <https://doi.org/10.1021/acsomega.3c00306>. [https://doi.org/10.1021/ACSOMEGA.3C00306/ASSET/IMAGES/LARGE/AO3C00306\\_0016.JPEG](https://doi.org/10.1021/ACSOMEGA.3C00306/ASSET/IMAGES/LARGE/AO3C00306_0016.JPEG).
- [49] Kulbak M, Cahen D, Hodes G. How Important Is the Organic Part of Lead Halide Perovskite Photovoltaic Cells? Efficient CsPbBr<sub>3</sub> Cells. *J Phys Chem Lett* 2015;6:2452–6. <https://doi.org/10.1021/acs.jpcclett.5b00968>. [https://doi.org/10.1021/ACSJPCCLETT.5B00968.SUPPL\\_FILE/JZ5B00968\\_SI\\_001.PDF](https://doi.org/10.1021/ACSJPCCLETT.5B00968.SUPPL_FILE/JZ5B00968_SI_001.PDF).
- [50] Shao JY, Li D, Shi J, Ma C, Wang Y, Liu X, et al. Recent progress in perovskite solar cells: material science. *Sci China Chem* 2023;66:10–64. <https://doi.org/10.1007/S11426-022-1445-2>. <https://doi.org/10.1007/S11426-022-1445-2/METRICS>.
- [51] Shao Z, Meng H, Du X, Sun X, Lv P, Gao C, et al. Cs<sub>4</sub>PbI<sub>6</sub>-Mediated Synthesis of Thermodynamically Stable FA<sub>0.15</sub>Cs<sub>0.85</sub>PbI<sub>3</sub> Perovskite Solar Cells. *Advanced Materials* 2020;32:2001054. <https://doi.org/10.1002/adma.202001054>.
- [52] Chang X, Fang J, Fan Y, Luo T, Su H, Zhang Y, et al. Printable CsPbI<sub>3</sub> Perovskite Solar Cells with PCE of 19% via an Additive Strategy. *Advanced Materials* 2020;32:2001243. <https://doi.org/10.1002/adma.202001243>.
- [53] Sutton RJ, Eperon GE, Miranda L, Parrott ES, Kamino BA, Patel JB, et al. Bandgap-Tunable Cesium Lead Halide Perovskites with High Thermal Stability for Efficient Solar Cells. *Adv Energy Mater* 2016;6:1502458. <https://doi.org/10.1002/aenm.201502458>.
- [54] Liu F, Ding C, Zhang Y, Ripolles TS, Kamisaka T, Toyoda T, et al. Colloidal Synthesis of Air-Stable Alloyed CsSn<sub>1-x</sub>Pb<sub>x</sub>I<sub>3</sub> Perovskite Nanocrystals for Use in Solar Cells. *J Am Chem Soc* 2017;139:16708–19. <https://doi.org/10.1021/jacs.7b08628>. [https://doi.org/10.1021/jacs.7b08628.SUPPL\\_FILE/JA7B08628\\_SI\\_001.PDF](https://doi.org/10.1021/jacs.7b08628.SUPPL_FILE/JA7B08628_SI_001.PDF).
- [55] Ling X, Zhou S, Yuan J, Shi J, Qian Y, Larson BW, et al. 14.1% CsPbI<sub>3</sub> Perovskite Quantum Dot Solar Cells via Cesium Cation Passivation. *Adv Energy Mater* 2019;9:1900721. <https://doi.org/10.1002/aenm.201900721>.
- [56] Houari M, Bouadjem B, Haid S, Matougui M, Lantri T, Aziz Z, et al. Semiconductor behavior of halide perovskites AGeX<sub>3</sub> (A = K, Rb and Cs; X = F, Cl and Br): first-principles calculations. *Indian Journal of Physics* 2020;94:455–67. <https://doi.org/10.1007/S12648-019-01480-0>. <https://doi.org/10.1007/S12648-019-01480-0/TABLES/5>.
- [57] Hamideddine I, Zitouni H, Tahiri N, El Bounagui O, Ez-Zahrouy H. A DFT study of the electronic structure, optical, and thermoelectric properties of halide perovskite KGeI<sub>3-x</sub>Br<sub>x</sub> materials: photovoltaic applications. *Appl Phys A Mater Sci Process* 2021;127:1–7. <https://doi.org/10.1007/S00339-021-04600-Y>. <https://doi.org/10.1007/S00339-021-04600-Y/FIGURES/6>.
- [58] Mahmood Q, Noor NA, Rashid M, Haq BU, Laref A, Qasim I. Physical properties of alkali metals-based iodides via Ab-initio calculations. *J Phys Chem Solids* 2019;132:68–75. <https://doi.org/10.1016/j.jpcs.2019.04.005>.
- [59] Luo Y, Tian H, Li X, Chen L, Yang Y, Wu D. Diversity of structural phases in AGeX<sub>3</sub> halides. *Phys Rev B* 2022;106:024112. <https://doi.org/10.1103/physrevb.106.024112>. <https://doi.org/10.1103/physrevb.106.024112/FIGURES/7>. <https://doi.org/10.1103/physrevb.106.024112/MEDIUM>.
- [60] Yu ZL, Ma QR, Liu B, Zhao YQ, Wang LZ, Zhou H, et al. Oriented tuning the photovoltaic properties of  $\gamma$ -RbGeX<sub>3</sub> by strain-induced electron effective mass mutation. *J Phys D Appl Phys* 2017;50:465101. <https://doi.org/10.1088/1361-663/aa8bea>.
- [61] Minemoto T, Murata M. Device modeling of perovskite solar cells based on structural similarity with thin film inorganic semiconductor solar cells. *J Appl Phys* 2014;116. <https://doi.org/10.1063/1.4891982>. <https://doi.org/10.1063/1.4891982/363801>.
- [62] Kavan L, Grätzel M. Highly efficient semiconducting TiO<sub>2</sub> photoelectrodes prepared by aerosol pyrolysis. *Electrochim Acta* 1995;40:643–52. [https://doi.org/10.1016/0013-4686\(95\)90400-W](https://doi.org/10.1016/0013-4686(95)90400-W).
- [63] Zheng H, Liu G, Zhang C, Zhu L, Alsaedi A, Hayat T, et al. The influence of perovskite layer and hole transport material on the temperature stability about perovskite solar cells. *Solar Energy* 2018;159:914–9. <https://doi.org/10.1016/j.solener.2017.09.039>.
- [64] Azri F, Meftah A, Sengouga N, Meftah A. Electron and hole transport layers optimization by numerical simulation of a perovskite solar cell. *Solar Energy* 2019;181:372–8. <https://doi.org/10.1016/j.solener.2019.02.017>.
- [65] Pandey R, Chaujar R. Numerical simulations: Toward the design of 27.6% efficient four-terminal semi-transparent perovskite/SiC passivated rear contact silicon tandem solar cell. *Superlattices Microstruct* 2016;100:656–66. <https://doi.org/10.1016/j.spmi.2016.10.033>.
- [66] Minemoto T, Murata M. Impact of work function of back contact of perovskite solar cells without hole transport material analyzed by device simulation. *Current Applied Physics* 2014;14:1428–33. <https://doi.org/10.1016/j.cap.2014.08.002>.
- [67] Makableh YF, Hassan W, Awad IA, Aljaioussi G. Comprehensive Electrical modeling analysis of Heterojunction Perovskite Solar Cells by using different electron transport nanostructured layers. *Superlattices Microstruct* 2021;150:106777. <https://doi.org/10.1016/j.spmi.2020.106777>.
- [68] Zandi S, Razaghi M. Finite element simulation of perovskite solar cell: A study on efficiency improvement based on structural and material modification. *Solar Energy* 2019;179:298–306. <https://doi.org/10.1016/j.solener.2018.12.032>.
- [69] Kalogirou SA. *Solar Energy Engineering: Processes and Systems*. 3rd ed. London, United Kingdom: Academic Press; 2023.
- [70] Siefert G, Bett AW. Analysis of temperature coefficients for III–V multi-junction concentrator cells. *Progress in Photovoltaics: Research and Applications* 2014;22:515–24. <https://doi.org/10.1002/pip.2285>.
- [71] COMSOL Multiphysics User's Guide. 2012. p. 1–1292.
- [72] Galagan Y, Coenen EWC, Verhees WJH, Andriessen R. Towards the scaling up of perovskite solar cells and modules. *J Mater Chem A Mater* 2016;4:5700–5. <https://doi.org/10.1039/C6TA01134A>.

- [73] Wenger S, Schmid M, Rothenberger G, Gentsch A, Grätzel M, Schumacher JO. Coupled optical and electronic modeling of dye-sensitized solar cells for steady-state parameter extraction. *J Phys Chem C* 2011;115:10218–29. [https://doi.org/10.1021/JP111565Q/SUPPL\\_FILE/JP111565Q\\_SI\\_001.PDF](https://doi.org/10.1021/JP111565Q/SUPPL_FILE/JP111565Q_SI_001.PDF).
- [74] Jung YS, Choi HW, Kim KH. Properties of p-type N-doped Cu<sub>2</sub>O thin films prepared by reactive sputtering. *Jpn J Appl Phys* 2014;53:11RA10. <https://doi.org/10.7567/JJAP.53.11RA10/XML>.
- [75] Rakic AD, Djurišić AB, Elazar JM, Majewski ML. Optical properties of metallic films for vertical-cavity optoelectronic devices. *Appl Opt* 1998;37:5271. <https://doi.org/10.1364/AO.37.005271>.
- [76] Behrouznejad F, Shahbazi S, Taghavinia N, Wu HP, Wei-Guang Diao E. A study on utilizing different metals as the back contact of CH<sub>3</sub>NH<sub>3</sub>PbI<sub>3</sub> perovskite solar cells. *J Mater Chem A Mater* 2016;4:13488–98. <https://doi.org/10.1039/C6TA05938D>.
- [77] Razza S, Di Giacomo F, Matteocci F, Cinà L, Palma AL, Casaluci S, et al. Perovskite solar cells and large area modules (100 cm<sup>2</sup>) based on an air flow-assisted PbI<sub>2</sub> blade coating deposition process. *J Power Sources* 2015;277:286–91. <https://doi.org/10.1016/J.JPOWSOUR.2014.12.008>.
- [78] Huang H, Shi J, Zhu L, Li D, Luo Y, Meng Q. Two-step ultrasonic spray deposition of CH<sub>3</sub>NH<sub>3</sub>PbI<sub>3</sub> for efficient and large-area perovskite solar cell. *Nano Energy* 2016;27:352–8. <https://doi.org/10.1016/J.NANOEN.2016.07.026>.
- [79] Giordano F, Abate A, Correa Baena JP, Saliba M, Matsui T, Im SH, et al. Enhanced electronic properties in mesoporous TiO<sub>2</sub> via lithium doping for high-efficiency perovskite solar cells. *Nat Commun* 2016;7:1–6. <https://doi.org/10.1038/ncomms10379>.
- [80] Anrango-Camacho C, Pavón-Ipiales K, Frontana-Urbe BA, Palma-Cando A. Recent Advances in Hole-Transporting Layers for Organic Solar Cells. *Nanomaterials* 2022; 12:443. <https://doi.org/10.3390/nano12030443>.
- [81] Kawano K, Pacios R, Poplavskyy D, Nelson J, Bradley DDC, Durrant JR. Degradation of organic solar cells due to air exposure. *Solar Energy Materials and Solar Cells* 2006;90:3520–30. <https://doi.org/10.1016/J.SOLMAT.2006.06.041>.
- [82] Li J, Qin J, Liu X, Ren M, Tong J, Zheng N, et al. Enhanced organic photovoltaic performance through promoting crystallinity of photoactive layer and conductivity of hole-transporting layer by V<sub>2</sub>O<sub>5</sub> doped PEDOT:PSS hole-transporting layers. *Solar Energy* 2020;211:1102–9. <https://doi.org/10.1016/J.SOLENER.2020.10.036>.
- [83] Sattari F, Mirershadi S, Shokri A, Mohammadi Sari Dargh4 M. The Effect of the Halogen Atoms on the Tuning the Band Gap in the Perovskite Structures. *Biquarterly Journal of Optoelectronic* 2017;1:51–8.
- [84] Mahmoud SA, Fouad OA. Synthesis and application of zinc/tin oxide nanostructures in photocatalysis and dye sensitized solar cells. *Solar Energy Materials and Solar Cells* 2015;136:38–43. <https://doi.org/10.1016/J.SOLMAT.2014.12.035>.
- [85] Wei X, Liu J, Liu XW. Ultrafine dice-like anatase TiO<sub>2</sub> for highly efficient dye-sensitized solar cells. *Solar Energy Materials and Solar Cells* 2015;134:133–9. <https://doi.org/10.1016/J.SOLMAT.2014.11.020>.
- [86] Lee KM, Lai CH, Chu WC, Chan SH, Suryanarayanan V. Thermal assisted blade coating methylammonium lead iodide films with non-toxic solvent precursors for efficient perovskite solar cells and sub-module. *Solar Energy* 2020;204:337–45. <https://doi.org/10.1016/J.SOLENER.2020.05.003>.
- [87] Song J, Yang Y, Zhao YL, Che M, Zhu L, Gu XQ, et al. Morphology modification of perovskite film by a simple post-treatment process in perovskite solar cell. *Materials Science and Engineering: B* 2017;217:18–25. <https://doi.org/10.1016/J.MSEB.2017.01.004>.